ChemPubSoc Europe
DOI: 10.1002/cssc.201600773
CHEMSUSCHEM Reviews

Charge Transport in Two-Photon Semiconducting Structures for Solar Fuels

Guohua Liu,[a, b] Kang Du,[a] Sophia Haussener,[c] and Kaiying Wang*[a]

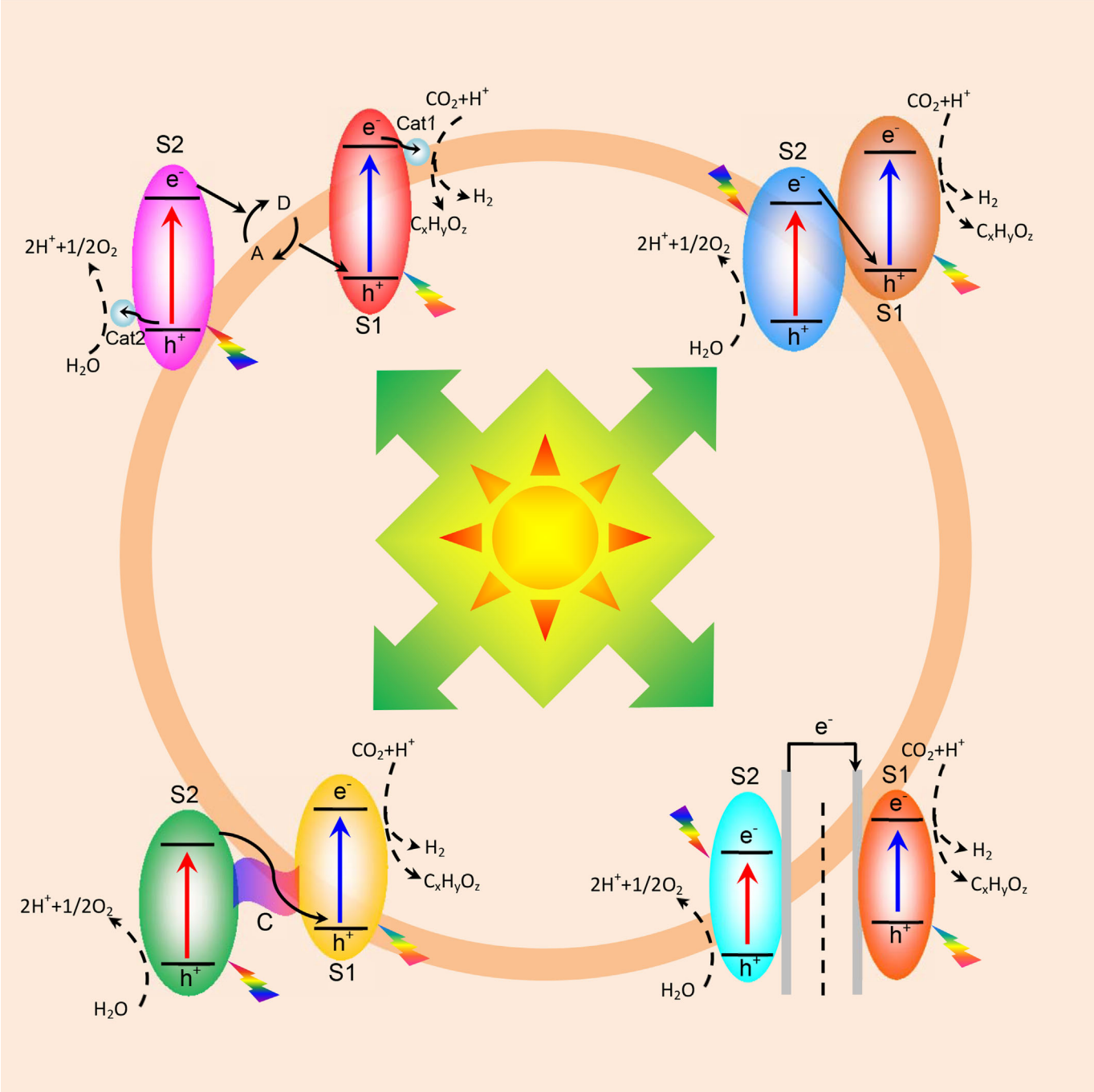

Semiconducting heterostructures are emerging as promising light absorbers and offer effective electron–hole separation to drive solar chemistry. This technology relies on semiconductor composites or photoelectrodes that work in the presence of a redox mediator and that create cascade junctions to promote surface catalytic reactions. Rational tuning of their structures and compositions is crucial to fully exploit their functionality. In this review, we describe the possibilities of applying the two-photon concept to the field of solar fuels. A wide range of strategies including the indirect combination of two semiconductors by a redox couple, direct coupling of two semiconductors, multicomponent structures with a conductive mediator, related photoelectrodes, as well as two-photon cells are discussed for light energy harvesting and charge transport. Examples of charge extraction models from the literature are summarized to understand the mechanism of interfacial carrier dynamics and to rationalize experimental observations. We focus on a working principle of the constituent components and linking the photosynthetic activity with the proposed models. This work gives a new perspective on artificial photosynthesis by taking simultaneous advantages of photon absorption and charge transfer, outlining an encouraging roadmap towards solar fuels.

1. Introduction

As the population increases and industrial growth continues, the energy demands of our society continue to rise. Nowadays, our major energy resources are still derived from limited and nonrenewable fossil fuels, such as coal, oil, and natural gas.[1] Their production and consumption are problematic. The by-products and chemicals used in the extraction and refinement of fossil fuels cause significant harm to the environment. The combustion of fossil fuels results in severe problems ranging from air and water pollution to global warming. Therefore, renewable energy sources are urgently needed to liberate our dependence on fossil fuels.

Solar energy provides a sustainable and clean resource. The challenge is to develop efficient methods to harvest and store solar energy.[2] This has stimulated studies to find materials capable of transforming solar energy into chemical fuels. Photochemical fuel production by water splitting or CO_2 reduction represents an attractive approach.[3] In this method, semiconductor photocatalysts or photoelectrodes (PEs) with assisting catalysts are integrated in photocatalytic (PC) or photoelectrochemical (PEC) devices.[4] The reactions are realized if sequential steps are accomplished: light harvesting to generate electron–hole pairs, charge separation and migration to the surface of the catalyst, and catalytic reaction between the charge carriers and the reactants.[3a,5] The overall efficiency is dependent on both the thermodynamics and the kinetics of the processes.

Photochemical conversion of solar energy is a fundamental research and technology challenge.[6] The basic problem lies in the coupling of the light-harvesting modules, which involves the catalysis of transient electron excited states to typically slow, multielectron, proton-coupled fuels.[3e,7] The technology challenge is integration of the complicated machinery responsible for this process, particularly the assembling and spatial structuring of the various components.[6c,8] Nature photosynthesis (NPS) provides a two-photon paradigm for doing this with molecular-based materials.[3b,9] To mimic the process, various structures have been proposed to simulate NPS through two separate semiconductors and a redox couple. The preferential attachment of redox species to a particular semiconductor surface is either an oxidation reaction or a reduction reaction.[10] Recently, advanced structures for fast charge transfer have been used for the process. For example, two different semiconductors through a heterojunction have been shown to induce swift electron transfer between materials,[11] ternary-component structures with a solid-state electron mediator are able to realize a vectorial electron-transfer path,[12] and various composite photoanodes[13] and cathodes[14] have been constructed for fuel generation. PEC devices employing multijunction photovoltaics (PVs)[15] or consisting of hydrogen- and oxygen-evolving electrodes[16] are also reported.

Although these efforts have been summarized in excellent reviews from specific aspects, for example, two-step solution contact systems,[17] composite photocatalysts and PEs,[3f,4b,5a,18] and solar-fuel devices,[19] the integration of materials for both photon absorption and charge transport remains poorly understood.[20] We believe that a comprehensive overview on ways to introduce the two-photon strategy for solar fuels is timely to promote further developments in this exciting field. In this work, we provide insight into two-photon semiconducting structures to understand interfacial carrier dynamics. Models are extracted from the literature to elucidate the mechanism of charge transport and to rationalize the experimental observations. We examine the physical explanations and attempt to distinguish ambiguities behind the models. Special focus is put on the techniques used to couple the materials and the working principle of the constituent components. Links between their performance and the proposed models are highlighted.

[a] *Dr. G. Liu, K. Du, Prof. K. Wang*
Department of Micro and Nano Systems Technology
University College of Southeast Norway
Horten, 3184 (Norway)
E-mail: Kaiying.Wang@hbv.no

[b] *Dr. G. Liu*
School of Energy and Environment
Anhui University of Technology
Maanshan, 243002 (PR China)

[c] *Dr. S. Haussener*
Institute of Mechanical Engineering
Ecole Polytechnique Federale de Lausanne
1015 Lausanne (Switzerland)

Guohua Liu received his Ph.D. degree in the Engineering of Thermophysics from the Chinese Academy of Sciences in 2010. He obtained his second Ph.D. degree in Micro and Nano Systems Technology at the University College of Southeast Norway (HSN) in 2013. He is currently a professor of Power Engineering at the Anhui University of Technology and a postdoctoral fellow working under the supervision of Prof. Kaiying Wang at HSN. His research interests are centered on the development and assembly of nanostructured materials for energy applications.

Kang Du is currently a PhD candidate at the University College of Southeast Norway (HSN) under the supervision of Prof. Kaiying Wang. He received his M.Sc. degree in Micro and Nano System Technology in 2014 at HSN, Norway. His present scientific interests focus on nanomaterials and photocatalysts for energy conversion and applications.

Dr. Sophia Haussener is an assistant professor and the head of the Laboratory of Renewable Energy Science and Engineering at École polytechnique fédérale de Lausanne (EPFL), Switzerland. She has worked in collaboration with numerous international partners on highly multi-disciplinary projects conducting investigations of transport phenomena in complex multi-phase media relevant to energy conversion technologies. A special focus lies on solar-driven energy conversion processes based on solar thermal, thermochemical, and electrochemical processes.

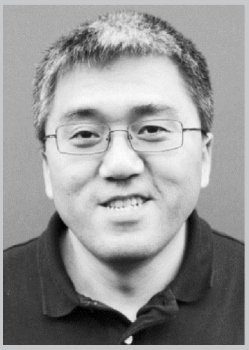

Kaiying Wang received his Ph.D. degree in Condensed Matter Physics from the Institute of Physics, Chinese Academy of Sciences, in 1995. He was a postdoctoral researcher at the University of New Orleans, USA. He joined the University College of Southeast Norway in 2007 as an associate professor and was then promoted to professor in 2010. His research interests focus on microfabrication and nanotechnology, functional thin films, magnetic and superconductive materials, nanostructure characterization, and nanodevices for environmental and energy applications.

2. Concept, Models, and Benefit of Two-Photon Structures

Plants use sunlight as an energy source and CO_2 and water as feedstock to split water as molecular oxygen, which is accompanied by the reduction of CO_2 to carbohydrates.[9a] The reactions occur over two distinct stages. The light reaction occurs through a stepwise electron-transfer process to accumulate sufficient energy for the chemical reaction (Scheme 1 a),[3b,9a,21] for which two photosystems (PSI and PSII) collect solar energy through an assembly of light-harvesting chlorophylls and power electrons to a higher electronic state inside the reaction center. At the donor side of PSII, water oxidation occurs on a manganese calcium oxide cluster. Electrons are extracted from water and are further donated to the lower oxidized form of P680. P680 is a pigment that absorbs $\lambda = 680$ nm light in PSII. Absorption of a photon excites P680 to P680*, at which the electrons are promoted to an actively reducing species. P680* donates its electron to the quinone--cytochrome f chain with proton pumping. The electron from cytochrome f is donated to PSI, which converts P700 into P700* (P700 is a pigment that absorbs $\lambda = 700$ nm light in PSI).The electrons along

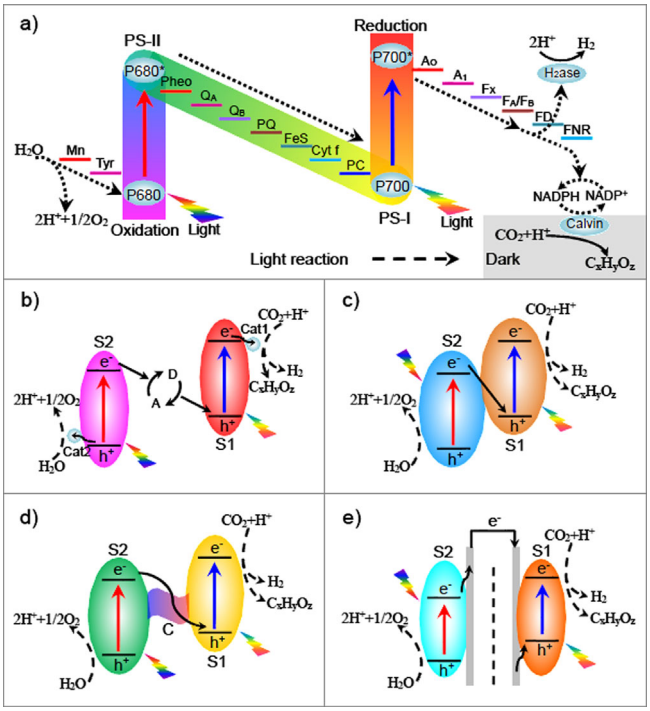

Scheme 1. a) Z-Scheme in natural photosynthesis for charge separation. P680: pigment that absorbs $\lambda = 680$ nm light in photosystem II; P680* is the excited state of P680; P700: pigment that absorbs $\lambda = 700$ nm light in photosystem I; P700* is the excited state of P700. Mn is manganese calcium oxide cluster; Tyr is tyrosine in PSII; Pheo is pheophytin, the primary electron acceptor of PSII; Q_A is primary plastoquinone electron acceptor; Q_B is secondary plastoquinone electron acceptor; PQ is plastoquinone; FeS is Rieske iron sulfur protein; Cyt f is cytochrome f; PC is plastocyanin; A_O is primary electron acceptor of PSI; A_1 is phylloquinone; F_X, F_A, and F_B are three separate iron sulfur centers; F_D is ferredoxin; FNR is nicotinamide adenine dinucleotide phosphate (NADP) reductase (adapted from refs. [3b, 21a, c]). Artificial two-photon structures of b) solution contact, c) direct contact, d) multicomponent, and e) photoelectrochemical cells.

with others are transferred to nicotinamide adenine dinucleotide phosphate ($NADP^+$) to form NADPH. Lastly, the dark reactions occur, during which the products of the light reaction form the C–C covalent bonds of carbohydrates. In this process, pigments absorbing a wide range of the visible spectrum convert light into chemical energy at PSII. Charge recombination is prevented by the presence of a transport chain, which drives electrons to PSI. Additional light harvesting takes place at PSI, which provides more energy to the electrons for their final purpose. This excitation cascade with electrons shuttled through the transport chain initiates the concept of two-photon structures.[21c,22]

Artificial two-photon structures are analogous to the electron-transport chain in NPS. According to the charge-extraction scheme, the structures are classified into four models: indirect combination of two semiconductors by redox couples (S1-A/D-S2) (Scheme 1 b), direct coupling of two semiconductors (S1-S2) (Scheme 1 c), multicomponent structure with a solid conductive mediator (S1-C-S2) (Scheme 1 d), and related PEs and two-photon cells (i.e., PEC) (Scheme 1 e). Here, the symbol S represents the semiconductor, A/D is the redox couple, and C represents the conductive material. The band gaps and band positions for a variety of semiconducting materials are depicted in Figure 1.[23] For H_2 evolution and CO_2 reduction, the position of the conduction band (CB) edge should be higher than the redox potential of H_2/H_2O or CH_4/CO_2 (CH_3OH/CO_2, HCHO/CO, $HCOOH/CO_2$, or CO/CO_2), whereas the position of the valence band (VB) edge should be lower than the redox potential of O_2/H_2O.[3a,c,24] The core of this concept is to steer charge transport between various materials and species. The engineering of energy bands and the interfaces of structures play important roles in the design of materials. The ultimate goal is to enhance light absorption and charge transfer to accelerate the photosynthetic reaction.

The essence of a two-photon structure lies in the coupling of different materials to efficiently capture and stabilize the energy of solar radiation to drive multielectron chemistry.[10b,11b,16] The electron transfer is balanced through an electron relay material between the absorbers. The process utilizes lower energy photons of the solar spectrum and increases the choices available for combinations of the materials. As long as the excited-state oxidation potential at the oxygen-evolving site (S2 in Scheme 1) is more negative than the excited-state reduction potential at the hydrogen-evolving site (S1), there is no further potential requirement for these states.[3b,18a] The system features spatial separation of charge carriers and enhances the stability of the catalyst against photocorrosion. The electrons aggregated in the CB of S1 produce an electron-rich region that suppresses photooxidation. Aggregation of the holes in the VB of S2 produces a hole-rich region, which protects S2 from photoreduction.

3. Principle, Materials, and Performance of Two-Photon Structures

3.1. Indirect combination of two semiconductors by a redox couple (photocatalytic systems)

The structure represents a system with two separate semiconductors in a solution redox mediator (Figure 2 a).[10a] Each semiconductor is responsible for one half-reaction, and the soluble redox mediator helps electron transfer between the materials.[17,25] Forward reactions occurring on the surface of S1 include reduction of protons by the CB electrons and oxidation

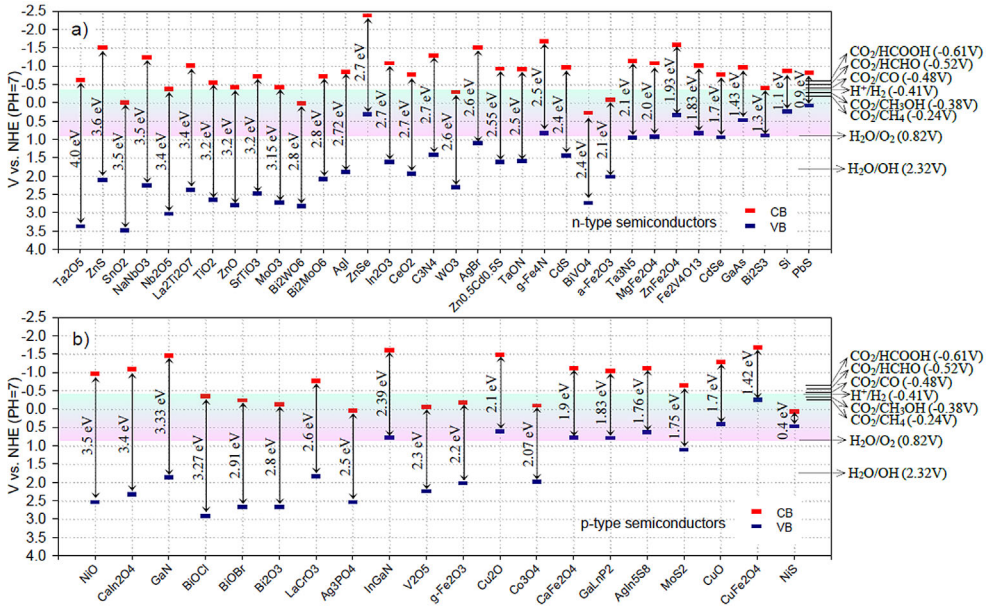

Figure 1. Band gaps and band positions of a) n-type semiconductors and b) p-type semiconductors relative to the redox potentials of various compounds involved in water splitting and CO_2 reduction. Values were taken from references given in the article. Note: The CB potential of a semiconductor material in aqueous solution usually exhibits a pH dependence described according to $E_{CB} = E^0_{CB\ (pH\ 0)} - 0.059\,pH$. The redox potentials of water also have the same linear pH dependence with a slope of 0.059 V per pH.

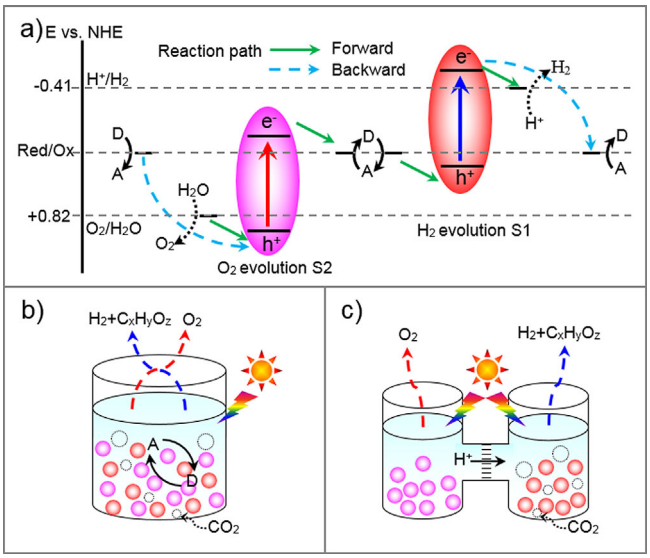

Figure 2. a) Energy diagrams of a solution contact system (adapted from ref. [10a]). b) Photocatalysts mixed in a conventional reactor. c) Twin reactor for product separation.

of the electron donor (D) by VB holes to yield the corresponding electron acceptor (A). The forward reaction on S2 is water oxidation, which occurs with the VB holes, and the A generated by S1 is converted into its reduced form (i.e., D). Thus, a cycle of redox pairs occurs and fuel production is fulfilled. The properties of the semiconductor, the cocatalyst (cat1 and cat 2 in Scheme 1 b), and the redox couple are key factors affecting the activity.

3.1.1. Semiconductors and cocatalysts

Since Bard introduced the concept of pairing semiconductors for water splitting,[26] many efforts have been made to develop new materials.[17] Many metal oxides and (oxy)nitrides have been reported for H_2 or O_2 evolution under UV/Vis light irradiation.[17b] The combination of Pt-TaON (H_2 evolution) and PtO_x/WO_3 (O_2) through the IO_3^-/I^- redox couple shows water splitting with an apparent quantum yield (AQY) of 0.5% under the illumination of $\lambda = 420$ nm UV light. Fuel production is stable, and stoichiometric amounts of H_2 and O_2 are produced within 60 h.[27] Between $\lambda = 520$ and 600 nm, RuO_2-loaded TaON nanoparticles (NPs)[10a] and Ir-loaded rutile TiO_2/Ta_3N_5 (oxy)nitrides[28] show functionality for O_2 evolution in the presence of the IO_3^-/I^- redox mediator. By extending the absorption wavelength further to $\lambda = 660$ nm, $BaZrO_3$/$BaTaO_2N$ with Pt NPs can be used as a water reduction promoter with either PtO_x/WO_3 or TiO_2 rutile as the O_2 evolution catalyst.[29] It is anticipated that nanosheets such as g-C_3N_4, $BiVO_4$, and WO_3 can be used and optimized to build more efficient systems under visible light.

The oxide $SrTiO_3$ exhibits high stability, but it alone cannot split water under visible light. Pairing Ru/Na,V-$SrTiO_3$, and Ru/Rh-$SrTiO_3$ with the aid of the IO_3^-/I^- mediator results in water splitting owing to narrowing of the band gap of the oxide by adjusting the impurity levels of the V 3d and Rh 4d states in the forbidden band. These intermediate energy levels act either as electron acceptors or donors that allow Ru/Rh-$SrTiO_3$ to reduce H_2O to H_2 and the holes in the VB of Na,V-$SrTiO_3$ to oxidize H_2O to produce O_2.[30] Inorganic modification and organic dyes are normally employed to tune the energy levels of the semiconductors for visible-light absorption. As organic dye sensitizers, NKX 2677 can be loaded on Pt(in)/$H_4Nb_6O_{17}$ for H_2 evolution and WO_3 for O_2 evolution with the IO_3^-/I^- redox couple between them; H_2 evolution proceeds at a steady rate of approximately 8 μmol h^{-1}.[31] Rapid electron injection from the anchored dyes into the semiconductor is responsible for this high performance.

Inorganic noble metals (Pt, Rh) and several metal oxides (NiO_x, RuO_2) are important cocatalysts to collect charge carriers. They are dispersed on a photocatalyst surface to provide active sites and to reduce the activation energy (Scheme 1 b).[4a, 32] The $SrTiO_3$:Rh system loaded with various cocatalysts (Ni, Ru, Rh, Pt, and Au) has been explored for H_2 evolution in the Fe^{3+}/Fe^{2+} electron-mediator solution.[32b] The activity using a Ru cocatalyst is as high as that using a Pt cocatalyst. The backwards reaction of water formation from H_2 and O_2 and the reduction of Fe^{3+} ions by H_2 do not proceed in the system. The (Ru/$SrTiO_3$:Rh)-(Fe^{3+}/Fe^{2+})-($BiVO_4$) system shows a quantum yield of 0.3% with stable activity for more than 70 h. The way in which the catalyst is synthesized is also an important factor affecting the AQY; it increases from 0.4 to 3.9–4.2% at $\lambda =$ 420 nm if $SrTiO_3$:Rh is synthesized by the hydrothermal and polymerizable complex method instead of a solid-state reaction.[33]

3.1.2. The redox couple and engineering aspect

Redox mediators inhibit the unfavorable recombination of electrons and holes, which is analogous to the transport chain in NPS. They transfer electrons from the O_2 evolution catalyst (OEC) to the hydrogen evolution catalyst (HEC) and are in direct contact with the catalyst surface. Many transition-metal complexes have been accepted as electron mediators including IO_3^-/I^-, Fe^{3+}/Fe^{2+}, $[Co(bpy)_3]^{3+/2+}$ (bpy = 2,2′-bipyridyl), $[Co(phen)_3]^{3+/2+}$ (phen = 1,10-phenanthroline), and NO_3^-/NO_2^-.[17b,34] The most common redox couples are IO_3^-/I and Fe^{3+}/Fe^{2+}, the former of which is used over a wide range of pH conditions and has no absorption in the visible-light region. Iodide salts (e.g., NaI) are used to initiate water splitting. By increasing the concentration of NaI, the efficiency of I^- oxidation by the VB holes for a HEC is increased, which results in water reduction to give more H_2. In the case of the Fe^{3+}/Fe^{2+} couple, the situation is similar, but the available pH range is limited to acidic conditions, because iron ions undergo precipitation to give iron hydroxide under neutral conditions. The cobalt complexes $[Co(bpy)_3]^{3+/2+}$ and $[Co(phen)_3]^{3+/2+}$ have been shown to be effective mediators. Their activity depends on the solution pH, and the highest activity is obtained under neutral pH conditions.[34] Nevertheless, all redox mediators absorb light to some extent and have limited long-term stability.

Nanoparticle photocatalysts are often mixed with an aqueous solution in a single reactor (Figure 2 b).[19c] In this reactor,

the backwards reaction occurs and separation of the products causes extra expense. A two-compartment system connected by a Pt wire with bromide and iron ions as electron mediators was proposed for water splitting in 1998.[35] Fuel production was then achieved in a dual-bed operation with O_2 evolution on WO_3 and H_2 evolution on $Pt/SrTiO_3$:Rh in an aqueous Fe^{2+}/Fe^{3+} solution.[36] Twin reactors also have been designed for CO_2 reduction.[37] Here, a fuel-evolving catalyst and an oxidation reaction catalyst are placed in different compartments of the reactor that are separated by a proton-exchange membrane (PCM, Figure 2c). Comparing the single catalyst $Pt/CuAlGaO_4$ system with the dual catalyst $Pt/SrTiO_3$:Rh and $Pt/CuAlGaO_4$ system in Fe^{2+}/Fe^{3+} solution, the dual-catalyst system shows a photoreduction quantum efficiency of 0.0051%, which is more than double the efficiency of the single-catalyst system.[37b] These reactors offer a viable prototype for engineering applications.

3.2. Direct coupling of two semiconductors (photocatalytic systems)

Loading one semiconductor onto another creates a semiconductor junction.[5c,18b,23] The band offsets and the electronic structure/affinity and work functions of the materials define the charge dynamics. According to energy level and band-gap alignment, the junctions are classified as injection sensitization (Figure 3a,b), p–n junction (Figure 3c,d), staggered (Figure 3c,d), straddling junction (Figure 3e), and direct Z-scheme (Figure 3f). These structures provide an offset of band edges that promotes spatial separation of the charges by transferring electrons in the higher CB to the lower CB and/or holes in the lower VB to the higher VB.

3.2.1. Injection sensitization

Injection sensitization happens in a system with a wide-band-gap semiconductor (S2) and a narrow-band-gap semiconductor (S1). The narrow-band-gap sensitizer is excited under visi-

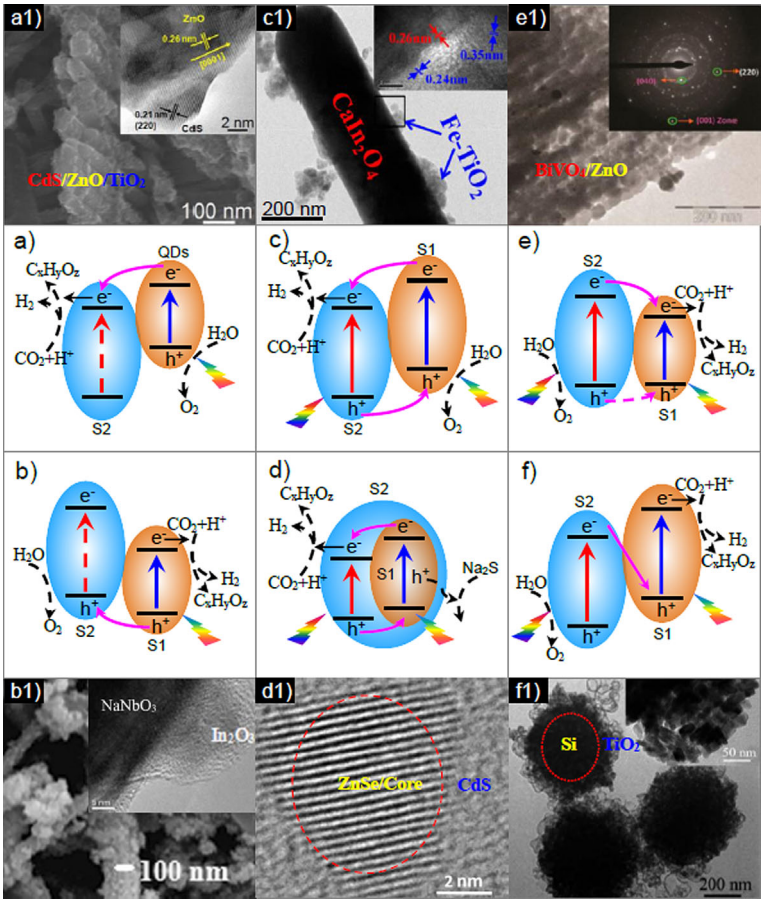

Figure 3. a) Electron-injection sensitization and its example a1) SEM and HRTEM images of A-TiO_2/ZnO/CdS (adapted from ref. [42], copyright 2014 Nature Publishing Group). b) Hole-injection sensitization and its example b1) SEM and TEM images of $In_2O_3/NaNbO_3$ rods (adapted from ref. [44], copyright 2010 American Chemical Society). c) The p–n junction and its example c1) TEM and HRTEM images of $CaIn_2O_4$/Fe-TiO_2 composite (reprinted with permission from ref. [11b], copyright 2014 American Chemical Society). d) Core–shell staggered junction and its example d1) TEM images of ZnSe/CdS nanocrystals (reprinted with permission from ref. [80], copyright 2012 American Chemical Society). e) Straddling junction and its example, e1) TEM images and SAED pattern of $BiVO_4$/ZnO (adapted from ref. [81], copyright 2014 American Chemical Society). f) Direct Z-scheme and its example, f1) SEM and TEM images of Si/TiO_2 nanospheres (adapted from ref. [100a], copyright 2014 American Chemical Society).

ble light and generates electrons and holes (Figure 3a, b).[38] The CB energy level of S2 is lower than that of the sensitizer (Figure 3a). Therefore, the electrons in the sensitizer can migrate to the CB of S2. For instance, the band gap of CdS is approximately 2.40 eV, and the CB and VB energy levels are approximately −0.50 and 1.90 eV versus normal hydrogen electrode (NHE). The electrons of CdS are transferred from the VB to the CB, whereas TiO_2 cannot be photoexcited under visible light because of its large band gap.[39] As a result, the electrons of CdS are injected into the CB of TiO_2, because the CB potential of CdS is more negative than that of TiO_2 (≈−0.26 eV). The holes remain in the VB of CdS owing to the lower positive potential of the CB.

Photoexcited electrons of CdS have been reported to inject into diverse nanostructures, such as elongated nanocrystals (NCs),[39] porous or layered materials,[40] and tubular semiconductor hosts.[41] The H_2 production rate of CdS/elongated TiO_2 NCs reaches 3.85 mmol h^{-1} g^{-1} if the Cd/Ti molar ratio is 0.17.[39] The H_2 generation rate of the CdS NPs with layered titanate nanosheets (≈1.0 mmol g^{-1} h^{-1}) is higher than that of their reference (≈0.13 mmol g^{-1} h^{-1} for bulk CdS/TiO_2).[40a] Strong electronic coupling between the 2D layered titanate nanosheets and the CdS NPs leads to a high visible-light harvesting ability, an increased charge lifetime, and expansion of the surface area. Decorating CdS NPs approximately 2–5 nm in size inside TiO_2 nanotubes (TNTs) not only promotes the H_2 evolution activity but also enhances the stability of CdS.[41b,c] CdS-coated TNTs undergo rapid deactivation after a reaction time of 4 h. However, the activity is stable for 13 h if CdS is confined within the TNTs. Figure 3a1 shows hierarchical structured CdS-sensitized 1D ZnO nanorods (NRs) on a 2D TiO_2 nanosheet; it exhibits better H_2 evolution performance (≈13.3 μmol h^{-1} cm^{-2}) than CdS-sensitized 1D ZnO/TiO_2 NRs.[42] This is due to efficient light harvesting and effective charge transport through the connected 3D network.

Hole injection is an inverse process to the electron injection, in which excitation of the sensitizer results in transfer of the holes to the VB of the semiconductor for the oxidation reaction (Figure 3b). For Ag_3PO_4/$SrTiO_3$[43] and In_2O_3/$NaNbO_3$ NR composites,[44] the CB edge of the sensitizer (i.e., Ag_3PO_4 or In_2O_3) is lower than that of the parent catalyst, whereas the VB edge of the catalyst is higher than that of the sensitizer. Under visible light, electrons in the sensitizer are excited to its CB, which leaves holes in the VB. The holes of the sensitizer are transported to the catalyst (i.e., $SrTiO_3$ or $NaNbO_3$) through the interface, whereas the electrons retain in the CB of the sensitizer.[44,45] O_2 evolution has shown that a small amount of $SrTiO_3$ brings about an increase in the activity of Ag_3PO_4. The AQY reaches 16.2% if the molar ratio of $SrTiO_3$/Ag_3PO_4 is approximately 5%.[43] In_2O_3 exhibits a low activity for H_2 evolution in CH_3OH solution (1.7 μmol g^{-1} h^{-1}), and almost no H_2 is formed over $NaNbO_3$ (Figure 3b1).[44] However, their combination with an In molar percentage of 0.25 improves the H_2 formation rate to 16.4 μmol g^{-1} h^{-1}, which is approximately one order of magnitude higher than that of In_2O_3 alone.

Injection-sensitized catalysts have also been applied for CO_2 reduction, such as CdS, Bi_2S_3,[46] PbS,[47] and AgBr[48] coupled with TiO_2, ZnTe decorated with ZnO[49] and $SrTiO_3$.[50] CdS- or Bi_2S_3-sensitized TNTs show selective reduction of CO_2 into methanol. The yields of methanol on TNTs, CdS/TNTs, and Bi_2S_3/TNTs catalysts are 102.5, 159.5, and 224.6 μmol L^{-1}, respectively.[46] The selectivity arises from the potentials of the CBs of Bi_2S_3 and CdS, which are more negative than those of the six-electron reduction of CO_2, H_2CO_3, and CO_3^{2-} to methanol in water. Thus, regardless of whether CO_2 is in the form of H_2CO_3 or CO_3^{2-} in water, it is reduced to methanol. The spectral range of light absorption depends on the band gap, which can be tuned by adjusting the size of the photocatalyst.[51] PbS NPs with diameters of 3, 4, and 5 nm have been used to sensitize TiO_2 doped with Cu cocatalysts for CO_2 conversion.[47] Although the CB edge of bulk PbS is slightly lower than that of TiO_2, quantum confinement shifts the CB edge of the smaller PbS NPs to higher energies, which enables electron injection into TiO_2. The activity is clearly dependent on the size of PbS. The conversion rates of CO_2 over the composites with 3, 4, and 5 nm PbS are reported to be 0.45, 1.12, and 0.60 μmol g^{-1} h^{-1}, all of which are higher than the conversion rate over Cu/TiO_2. This is because smaller PbS NPs facilitate electron–hole separation, whereas particles with larger diameters extend the visible absorption owing to the smaller band gap.

3.2.2. P-n junction

The p-n junction is an interface between p-type and n-type semiconductors. Within the interface, the energy bands are bent and the Fermi levels are equilibrated to reach a new equilibration between diffusion and migration, which results in the formation of a space-charge region. The built-in potential in the space-charge region allows effective separation of the charges (Figure 3c).[18b,24,52] n-Type TiO_2 has been coupled with various p-type semiconductors to form these junctions, for example, $CuFe_2O_4$/TiO_2,[53] Cu_2O/TiO_2,[54] CuO_x/TiO_2,[55] $CaIn_2O_4$/Fe-TiO_2,[11b] and CuO/$TiO_{2-x}N_x$.[56] Figure 3c1 presents a TEM image of a $CaIn_2O_4$ NR with a tunable Fe-TiO_2 content. The composite leads to a H_2 evolution rate of 280 μmol g^{-1} h^{-1}, which is 12.3 times higher than that of pure $CaIn_2O_4$ and 2.2 times higher than that of pure Fe-TiO_2.[11b] The enhanced rate is attributed to increased surface area, enhanced visible-light absorption, and efficient charge separation across the interface. Porous Cu_2O/TiO_2 offers more reaction active sites than their composite particles for CO_2 conversion. The formation rate of CH_4 is 28.4 ppm g^{-1} h^{-1}, which is approximately 12, 9, and 7.5 times higher than that of the pure TiO_2, Pt/TiO_2, and commercial P25 powders.[54] As nitrogen atoms enter the lattice TiO_2, they make the band edges more compatible for charge transfer. The CuO-$TiO_{2-x}N_x$ composite with a hollow nanotube structure shows a high CH_4 formation rate of 41.3 ppm g^{-1} h^{-1} from CO_2 reduction.[56]

By depositing p-type NiS NPs onto n-type CdS NRs, the H_2 generation rate becomes higher than that of 1 wt% Pt-loaded CdS NRs.[57] The assembly of NiS NPs on the surface of CdS NRs results in the formation of a large number of p–n junctions that reduce charge recombination. The optimal NiS loading is 5 mol%, and the corresponding H_2 rate reaches

1131 μmol g^{-1} h^{-1}. However, cadmium suffers from photocorrosion and is toxic. The emerging perovskite n-$La_2Ti_2O_7$/p-$LaCrO_3$ evolves 267.6 μmol h^{-1} of H_2, whereas $LaCrO_3$ photocatalyst produces only 74.4 μmol h^{-1}.[58] This boost in activity is the result of the low recombination rate of the charge carriers and visible-light activation of $La_2Ti_2O_7$. A nanodiode of p-$CaFe_2O_4$ (≈1.9 eV) and n-$PbBi_2Nb_{1.9}W_{0.1}O_9$ (≈2.75 eV) has also been constructed.[59] This composite shows enhanced activity for both H_2 production in methanol solution and water oxidation in $AgNO_3$ solution. Similar bulk junctions of $CaFe_2O_4$/$MgFe_2O_4$ (2.0 eV) have also been reported.[60] The H_2 evolution rate of the RuO_2/$MgFe_2O_4$/$CaFe_2O_4$/Pt composite remains almost the same after several runs with a quantum yield of 10.1%. This performance comes from the effect of the junction, for which the p-type and n-type semiconductors are dispersed from each other.

3.2.3. Staggered alignment

For staggered band-gap heterostructures, both the CB and VB edges of S1 are higher than those of S2 (Figure 3c,d). The energy gradient existing at the interface tends to separate electrons and holes on different sides; the electrons are confined to the CB of S2 and the holes are confined to the VB of S1. Band bending resulting from the difference in the chemical potentials of the semiconductors also contributes to a built-in field. It remains under debate as to whether this occurs through electron transfer owing to favorable energetics of the relative positions of the CBs or through band bending at the interface.[5c,18b,23,61] As a result, spatially localized charges across the junction can participate in redox reactions. The disadvantage of this structure is weak redox ability after charge transfer.

One wide-band-gap semiconductor coupling to another narrow-band-gap semiconductor results in the formation of a junction, and this occurs in TiO_2/CeO_2,[62] TiO_2/ZnO,[63] Ta_2O_5/In_2O_3,[64] Cu$_2$O/g-C_3N_4,[65] In_2O_3/g-C_3N_4,[66] N-TiO_2/g-C_3N_4,[67] ZnO/g-C_3N_4,[68] TiO_2/SnO_2,[69] and TiO_2/Nb_2O_5.[70] Incorporation of In_2O_3 improves the thermal stability of mesoporous Ta_2O_5 and leads to a composite with a reduced band gap. The composite promotes electron transfer from the CB of In_2O_3 to the CB of Ta_2O_5, and the inverse transfer of the holes retards the recombination probability. A H_2 evolution rate of approximately 92 μmol g^{-1} h^{-1} is detected with a stability of approximately 30 h.[64] Recent studies focus on new photosystems such as metal nitrides and carbon nitrides. Fe_4N/Fe_2O_3 structures improve the separation of charges and enhance the water-splitting reaction.[71] First-principles analyses have revealed that the properties originate from particle-size-dependent changes in the band structure. The proximity of the VB potential of the component promotes the entrapment of hole carriers, and the defect-induced interband-gap energy states lead to effective charge separation. g-C_3N_4 is a metal-free semiconductor, and its CB band edge (−1.20 eV vs. NHE at pH 7) is more negative than that of TiO_2 (−0.29 eV), which implies that its photoexcited electrons have stronger reducibility, and this allows it to reduce CO_2 to CH_3OH. ZnO with a CB potential of −0.44 eV has moderate ability to absorb CO_2. Loading ZnO on porous g-C_3N_4 markedly increases the activity. Under sunlight for 1 h, the generation rates of ethanol, methane, methanol, and CO reach 2.5, 5.4, 19.0, and 38.7 μmol g_{cat}^{-1}. The optimal sample shows a CO_2 conversion rate of 45.6 μmol g^{-1} h^{-1}, which is 4.9 times higher than that of g-C_3N_4 and 6.4 times higher than that of P25.[68] An optimal concentration exists because if the loading of ZnO is too high it blocks the active sites on g-C_3N_4.

Multiple interfaces increase the complexity of charge transport, as in the Cu$_2$O@SnO_2@Fe_2O_3,[72] V_2O_5/$BiVO_4$/TiO_2,[73] and ZnS/CdS@Fe_2O_3[74] composites. One-dimensional Cu$_2$O@SnO_2@Fe_2O_3 core–double shells present a tubelike morphology and has broad spectral response to sunlight owing to the combination of a narrow-band-gap material (e.g., n-Fe_2O_3, ≈2.2 eV or p-Cu$_2$O, ≈3.6 eV) with wide-band-gap n-SnO_2 (≈3.6 eV).[72] The band structures of Cu$_2$O or Fe_2O_3 and SnO_2 match well with each other; the CB edge of Cu$_2$O or Fe_2O_3 is higher than that of SnO_2, and the VB edge of Cu$_2$O or Fe_2O_3 is lower than that of Cu$_2$O. Consequently, photoexcited electrons are transported to the surface of SnO_2, whereas the holes migrate to the surface of α-Fe_2O_3 or Cu$_2$O. Apart from charge transfer, stability is another key issue, in particular for long-term applications. Coating photoactive CdS and/or ZnS onto a magnetic Fe_2O_3 core results in stable and recyclable catalysts. CdS/Fe_2O_3, ZnS/Fe_2O_3, and ZnS/CdS@Fe_2O_3 core–shell catalysts can be synthesized by a co-precipitation method. ZnS/CdS@Fe_2O_3 evolves a higher volume of H_2 and is more stable than the other counterparts. The maximum H_2 production is 4129 μmol, which gives rise to a quantum efficiency of 19% at $\lambda = 510$ nm.[74] In this case, vectorial charge transfer is presumed over all the components for separation of charges, which thus enhances the activity.

Incorporating one or more elements into a parent semiconductor results in the formation of a homogenous solid solution, for example, mixing ZnS and CdS results in $Cd_{1-x}Zn_xS$. The band gap of the solid solution can be adjusted by tuning the Zn/Cd concentration ratio. Thus, coupling the solid solution with other materials, for example, Pt/$Cd_{1-x}Zn_xS$/ZnO/$Zn(OH)_2$,[75] $Cd_{0.5}Zn_{0.5}S$/g-C_3N_4,[76] and CdS/$Ba_{1-x}Zn_xTiO_3$,[77] offers a flexible technique for band-gap engineering. The activity of 1%Pt/$Cd_{0.2}Zn_{0.8}S$/ZnO/$Zn(OH)_2$ exceeds that of 1%Pt/$Cd_{0.1}Zn_{0.9}S$ by a factor of 2.[78] The highest H_2 production of approximately 2256 μmol g^{-1} h^{-1} is achieved by Pt/$Cd_{1-x}Zn_xS$/$Zn(OH)_2$ owing to the fact that its electron reduction potential for zinc hydroxide is higher than that of ZnO.[75] For the CdSe@ZnTe core–shell structure, one of the carriers is confined in the ZnTe core, and it is not accessible for surface reactions. However, if the thickness of the outer layer is modified with an appropriate charge-accepting moiety, the confined carriers can tunnel to the surface and can be regenerated by a scavenging agent.[79] The hole-scavenging surfactant facilitates transfer of core-localized holes to the surface, even for shells exceeding 7 nm in thickness (Figure 3d,d1).[80] The transfer of charge carries from the ZnSe core to the surface of the CdS shell is approximately one order of magnitude faster than the recombination time, which indicates that most of the absorbed energy is available to drive the catalytic reactions.

3.2.4. Straddling alignment

For a straddling band-gap alignment structure (Figure 3e), both the VB and CB edges of S1 are localized within the energy gap of S2. Photoexcited electrons are transferred from CB2 to CB1, and the holes are transferred from VB2 to VB1. All charge carriers are accumulated on S1, which does not affect the activity.[23] However, the potential difference between the materials is asymmetric in most cases. Specifically, the CB band edges of ZnO and $BiVO_4$ are situated at −0.38 and +0.32 eV versus NHE at pH 7, whereas the VB edges of $BiVO_4$ and ZnO are at +2.78 and +2.84 eV. The CB potential of $BiVO_4$ is much more positive (+0.7 eV) than that of ZnO, whereas the VB of $BiVO_4$ is slightly more negative (≈−0.06 eV) than the VB of ZnO. Thus, there is a greater tendency for the electrons to flow from ZnO to $BiVO_4$. As there is not much difference in the VB levels, the impetus for holes to flow into $BiVO_4$ is low (Figure 3e,e1).[81] This facilitates charge transfer, and the mechanism supports the design of $V_2O_5/BiVO_4$,[82] Bi_2S_3/CdS,[83] and $TiO_2/SrTiO_3$[84] composites. The Bi_2S_3/CdS composite has been shown to catalyze the reaction of CO_2 with H_2O to give methanol in a yield of 613 μmol g^{-1}; this value is approximately threefold higher than the yield given by the CdS parent and twofold higher than the yield produced by Bi_2S_3.[83] The TiO_2/$SrTiO_3$ catalyst produces approximately 4.9 times more H_2 than TiO_2 and 2.1 times more than $SrTiO_3$.[84b]

For core–shell NCs with a narrow band core, electron–hole pairs near the interface tend to be confined in the core. The separation and transfer of charges from the core to the outer shell surface is a challenging issue. In the cases of ZnS@CdS and ZnS@CdSe NCs, the surface-trap states are passivated by the ZnS shell. The confined electrons and holes with high energy in the core might tunnel through the shell to the outer surface.[85] A similar transfer has been observed in CdS@CdSe NCs, in which charge-carrier tunneling produces a 10-fold increase in H_2 evolution over the CdSe core NCs alone.[86] The inverted straddling-band-gap structure is found in a material with a narrower band gap grown epitaxially around the core material with a higher band gap,[87] and the charges are rationally driven to the shell by the built-in potential. For this reason, In_2S_3@In_2O_3 core–shells present a H_2 evolution rate of approximately 61.4 μmol g^{-1} h^{-1}.[88] On the other hand, chemical etching can be used to open the shell to expose the core to the external environment. The resulting morphology is desirable, as it can enable both the reductive and oxidative reactions to run simultaneously on different surfaces. The hydrogen production activity of CdSe@CdS can be improved three-to-fourfold by etching treatment.[89]

3.2.5. Direct Z-scheme

In the direct Z-scheme, a large number of defects aggregate at the semiconductor/semiconductor contact interface. The energy levels of the interface are quasicontinuous and show properties similar to those of conductors with low electric resistance. Thus, the contact interface serves as the center for charge recombination. The band alignment of the two semiconductors in the direct Z-scheme presents a staggered edge position, and the CB and VB of each semiconductor do not satisfy redox potential requirements for an overall reaction, but they can perform half-reactions separately (Figure 3f).[18a,38a,90] According to charge transfer, the electrons are required to combine with the same quantity of holes. The ideal case is that S1 and S2 produce the same number of charge carriers. This can be coordinated by tuning the mass ratio of the materials.[3b,18a] Whereas a broad contact interface promotes charge recombination, a balanced distribution of incident photons maximizes light absorption. Thus, architectural diversity in material systems also requires an optimal mass ratio.[91] The clear advantage of this separation lies in the availability of powerful reductive electrons and oxidative holes.

The direct Z-scheme has been successful in the design of catalysts. The 1 wt% Pt-loaded $(ZnO)_1/(CdS)_{0.2}$ catalyst shows the highest H_2 evolution rate of 1805 μmol g^{-1} h^{-1} among different reference structures; this value is 14 times higher than that of the CdS catalyst and 40 times higher than that of the ZnO catalyst.[91c,92] Relative to particles, CdS/ZnO nanowire arrays effectively trap light by extending the path length. The photoexcited electrons in a low CB of ZnO are injected into a higher VB of CdS and recombine with the holes to realize desirable reverse carrier transfer. The H_2 evolution rate is approximately 2.0 times that of CdS/ZnO NPs.[11a] $BiVO_4$-Ru/$SrTiO_3$:Rh,[93] WO_3/CdS,[94] WO_3/g-C_3N_4,[95] SiC/CdS,[96] Si/TiO_2 nanotree structures,[97] and rutile/anatase TiO_2 composites[91b] follow this Z-scheme mechanism. In the Ru/$SrTiO_3$:Rh-$BiVO_4$ system, interparticle electron transfer occurs from $BiVO_4$ to Ru/$SrTiO_3$:Rh.[93b] The impurity level (Rh^{3+}/Rh^{4+}) formed by doping in the forbidden gap of $SrTiO_3$ serves as a mediator and assists in electron transfer. The direct Z-scheme is also thought to exist at the anatase/rutile interface.[91b,98] The TiO_2 sample composed of 45 wt% rutile phase and 55 wt% anatase phase exhibits a H_2 production rate of 324 μmol h^{-1}.

A few studies report direct Z-schemes for CO_2 reduction,[91a,99] one of which involves the CuO/TiO_2 composite. The electrons of CuO are used for CO_2 conversion, and the holes from TiO_2 are consumed by the sacrificial reagent methanol. The interface favors the combination of holes from CuO and electrons from TiO_2. The optimal rate of methyl formate formation is reported to be approximately 1600 μmol g^{-1} h^{-1}.[99b] The CB band edge of $ZnFe_2O_4$ lies at −1.5 eV versus NHE at pH 7, which is higher than that of TiO_2 and is more negative than the redox potential of CO_2/HCOOH. The VB position of TiO_2 lies at 2.7 eV, which is more positive than that of the anodic oxidation of cyclohexanol. Thus, coupling TiO_2 with $ZnFe_2O_4$ is thermodynamically favorable for CO_2 reduction. The junction has higher activity than either pure $ZnFe_2O_4$ or TiO_2, and the composite with a 9.78% $ZnFe_2O_4$ content exhibits the highest yield.[91a] The Si(S1)/TiO_2(S2) composite (Figure 3f1) also presents activity in the conversion of CO_2 into methanol.[100] In this system, the potential barrier at the Si/TiO_2 interface reflects holes back into the TiO_2 layer, and the holes move toward the TiO_2/electrolyte interface and oxidize OH^- to oxygen. The electrons in Si moving to the surface trigger the CO_2 reducing reaction.

3.3. Multicomponent structures with a solid conductive mediator (photocatalytic systems)

In this structure, two semiconductors are bridged with a solid electron mediator or conductor (Scheme 1 d). The conductor shows a stronger ability for charge transfer than the solid contact interface among the semiconductors.[18,101] In theory, any conductor, including metals and graphene oxide, can serve as the conductive mediator.

3.3.1. Metal electron mediator

Metals in multicomponent structures can be functionalized as storage centers (Figure 4 a) and/or recombination centers (Figure 4 b, c), which contribute to charge separation and to enhancing interfacial carrier transport.[12a,18a,102] The metallic components may also enhance light absorption through a plasmonic effect (Figure 4 d–f).[103] With these mechanisms, the structures have the capability to generate holes with strong oxidation power and electrons with strong reduction power.

3.3.1.1. Electron capture center (Schottky junction)

Metal semiconductor catalysts are often prepared by loading metallic nanoclusters on a semiconductor surface. Contact of the metal with an n-type semiconductor creates a Schottky junction, at which the work function of the metal is slightly higher than that of the semiconductor. Upon excitation, photoexcited electrons from the semiconductor are transferred across the Schottky junction to the metal, which results in a shift in the Fermi level of the metal towards a new equilibrium (Figure 4 a).[102,104] In this manner, the metal acts like an electron sink to enable separation of electrons and holes, which thus extends the lifetime of the holes on the semiconductor surface for the oxidation reaction. Besides, the metal components provide active sites to reduce the overpotential for surface chemical reactions.

Typical cases of this type include CdS/TiO_2/Pt,[102,104b,105] $AgIn_5S_8$/TiO_2/Pt,[106] TNT/CdS/Pt,[107] CdS/PdS/Pt,[108] CdS/TiO_2/Au,[109] TiO_2/In_2O_3/Pt,[110] CdS/BN/Pt,[111] and IrO_2 or CoO_x/Ta_3N_5/Pt.[112] These systems show high activities that far exceed those of one- and two-component systems. The effects of Pt and PdS co-loaded on a metal sulfide [e.g., CdS or $ZnO_{1-x}S_x$,

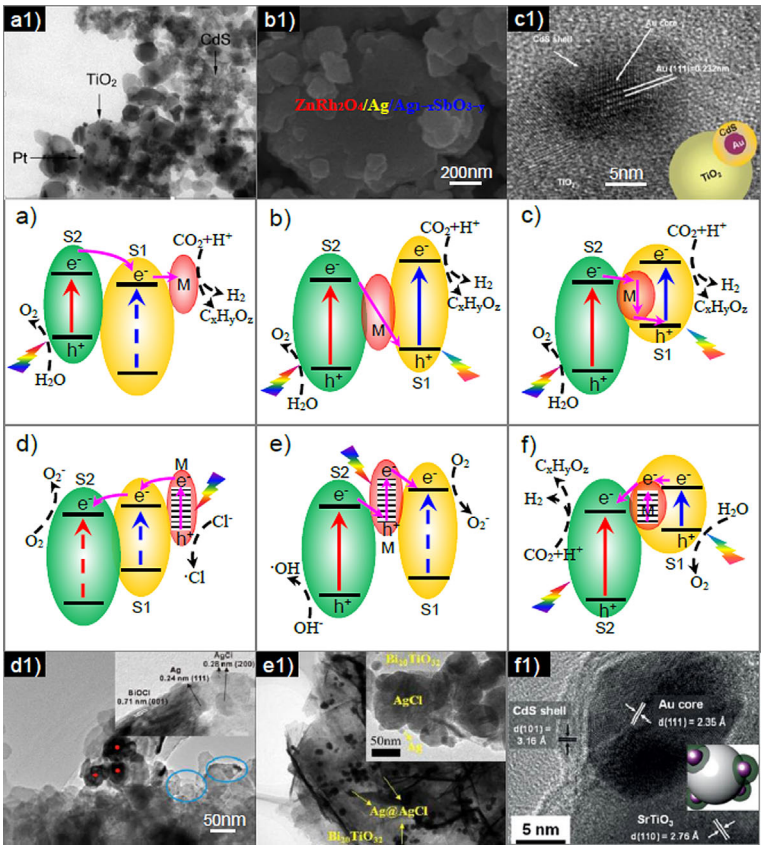

Figure 4. a) Metal acts as an electron capture center and its example, a1) TEM image of CdS/(Pt-TiO_2) (reprinted with permission from ref. [105a], copyright 2008 Royal Society of Chemistry). b) Metal acts as an electron recombination center and its example, b1) SEM images of $ZnRh_2O_4$/Ag/$AgSbO_3$ (reprinted with permission from ref. [133], copyright 2014 American Chemical Society). c) Metal acts as an electron recombination center in core–shell structures and its example, c1) HRTEM image of CdS/Au/N-TiO_2 heterostructures (reprinted with permission from ref. [137], copyright 2014 Elsevier). d–f) Metal acts as a plasmonic effect in parallel structures and their examples, d1) TEM and HRTEM images of Ag/AgCl/BiOCl (adapted from ref. [149i], copyright 2012 American Chemical Society); e1) TEM images of Ag-AgCl@$Bi_{20}TiO_{32}$ photocatalysts (reprinted with permission from ref. [149d], copyright 2013 American Chemical Society); f1) HRTEM image of the interface region of $SrTiO_3$ and Au@CdS (adapted from ref. [149e], copyright 2014 Wiley-VCH).

$ZnIn_2S_4$, $ZnGa_2S_4$, $(CuIn)_{0.8}Zn_{1.82}S$] have been studied for H_2 evolution.[108] The activities of the catalysts follow the order Pt/MS < PdS/MS < Pt/PdS/MS, and the best H_2 evolution rate of approximately 8800 μmol h^{-1} is obtained from the Pt/PdS/CdS catalyst. The activity indicates that PdS acts as an effective co-catalyst for oxidation, whereas Pt functions as an electron-trapping center for proton reduction. In principle, microporous zeolite Y loaded with Pt, TiO_2, CdS, and Pt/TiO_2 NPs are proposed for water splitting. The zeolites help to prevent aggregation of the nanoparticles and stabilize the structure, and provide access for the solution species to the zeolite-bound particles.[102] An additional study validates the use of Pt/CdS/TiO_2 composites within a hierarchically reticular structure, as H_2 is generated at a rate of approximately 118 μmol h^{-1} on this catalyst.[105b] Notably, the location of Pt on the catalyst is a critical factor affecting the efficiency, as the rate increases by a factor of 3–30 for CdS/(Pt-TiO_2) relative to that for Pt-(CdS)/TiO_2 (Figure 4a1).[104b,105a]

Rational integration of a light-absorber, hole and electron acceptor is important for charge transfer. The ZnSe/CdS/Pt[113] and CdSe/CdS/Pt[104a] hybrids are formed by coupling several crystalline materials. The three components with unique functionalities are assembled to form a linear energy gradient. The photoexcited carriers are steered to be localized in nonadjacent parts of the NR, the holes reside in the semiconductors, and the electrons reside in the metal domains.[113b] Spatial localization of the carriers suppresses backwards recombination, which leads to efficient harvesting of visible light through injection of electrons into metallic Pt. Lian et al. have examined the rate of elementary electron–hole separation and the recombination steps in CdSe/CdS-Pt and CdS-Pt NRs.[104a] The electron-transfer efficiencies to Pt are near 100% and hole transfer is the bottleneck step. The hole-transfer rates to the electron donor can be correlated with the quantum efficiency of H_2 generation.

Loading MgO on a Pt-TiO_2 photocatalyst can enhance CO_2 reduction.[114] The role of MgO is to attract CO_2 molecules onto the catalyst surface to destabilize the chemical bonds of CO_2 by the enriched area of electrons near the Pt nanoparticles. However, maintaining long-term stability of the catalyst is a challenge, as CO easily poisons Pt nanoparticles. One strategy to avoid poisoning is to use bimetallic alloys. Coaxial $SrTiO_3/TiO_2$ nanotube arrays loaded with Au–Cu bimetallic alloy NPs have been designed to reduce CO_2 into CO and hydrocarbons.[115] It is found that $Au_3Cu/SrTiO_3$/TNTs is the most reactive catalyst in the alloy family. A CO production rate of 3.77 mmol g^{-1} h^{-1} and a total hydrocarbon of 725.4 μmol g^{-1} h^{-1} are obtained. In the reaction, $N_2H_4{\cdot}H_2O$ as the H source and electron donor offers a reducing atmosphere to protect the surface Cu atoms against oxidation, which thus maintains the alloying effect for high activity and stability.

3.3.1.2. *Electron recombination center (ohmic junction)*

The interface between semiconductors contains an ample amount of defects that hamper charge transfer. Insertion of a conductor between the semiconductors forms an ohmic contact with low contact resistance.[18a,101b] The work function of the ohmic metal layer should match the band positions of the semiconductors, so that the photoexcited electrons from the CB of S2 recombine with the holes from the VB of S1 through the contact (Figure 4b,c). Although one photon is lost during this recombination, it reduces the distance of electron transfer and the remaining carriers can promote the redox reactions. In addition to physical separation of the redox sites, the ohmic junction offers net photon energies for the reactions by partial overlap of two band gaps.

Metals in the CdS/Ag/TNT,[116] Bi_2WO_6/Ag/N-TiO_2,[117] $SrTiO_3$:La-Rh/Ir/CoO_x-Ta_3N_5,[118] $SrTiO_3$:La-Rh/Au/$BiVO_4$,[119] $SrTiO_3$:La-Rh/Au/$BiVO_4$:Mo,[120] and CeO_2/Pt/SiO_2[121] composites have been functionalized as electron relay or recombination centers (Figure 4b). The high photocurrent of CdS/Ag/TNTs might be due to the efficient electron traps formed at the CdS–Ag junction.[116a] However, Xie et al. believe that two-step excitation between CdS and TiO_2 with Ag as a mediator induces electron vectorial transfer.[116b] The La-Rh:$SrTiO_3$/Ir/CoO_x-Ta_3N_5 material exhibits a rate of H_2 evolution that is 3.8 times higher than that of the $SrTiO_3$:Rh system. Introduction of Au as a mediator in the $SrTiO_3$:La-Rh/Au/$BiVO_4$ system results in a catalyst with high activity for overall water splitting. The activity using particulate semiconductors immobilized onto Au layers is approximately 6 times higher than that of a powder suspension and 20 times higher than that of the La-Rh:$SrTiO_3$/$BiVO_4$ system without metal layers.[110–120] The performance comes from the presence of a metallic conductor (e.g., Ir, Au layer), which serves as an electron shuttle to transfer electrons from one semiconductor to another effectively.

As one constituent element of the photocatalysts is same as the metallic mediator, such as in $W_{18}O_{49}$/Ag/AgCl,[122] Cu_2O/Ag/AgBr-Al_2O_3,[123] AgBr/Ag/TiO_2,[124] TNT/Ag/AgBr,[125] AgBr/Ag/Bi_2WO_6,[126] AgBr/Ag/g-C_3N_4,[127] AgBr/Ag/Bi_2MoO_6,[128] Ag_3PO_4/Ag/AgI,[129] Ag_3PO_4/Ag/WO_{3-x},[130] AgI/Ag/AgBr,[131] and AgBr/Ag/MoO_3,[132] there exists a concentration equilibrium between the metal and its ions. The intimate contact interface between the conductor and the catalyst presents low electric resistance that is beneficial for the formation of an ohmic contact. For example, water splitting has been performed on $ZnRh_2O_4$/Ag/$Ag_{1-x}SbO_{3-y}$, in which zinc rhodium oxide and defective silver antimonate act as the H_2 and O_2 evolution catalysts and Ag acts as an electron mediator for electron transfer (Figure 4b1).[133] Another case is Ag_3PO_4/Ag/g-C_3N_4,[134] in which metallic Ag NPs are involuntary formed on the interface under irradiation owing to photodecomposition of AgX. The optimal sample shows a CO_2 conversion rate of 57.5 μmol g^{-1} h^{-1}, which is 6.1 times higher than that of g-C_3N_4 and 10.4 times higher than that of P25. Different from the in situ generation of the electron mediator, the catalyst can be inversely formed from a chemical reaction of the metallic mediator. As in the preparation of the ZnO/Cd/CdS and WO_3/W/$PbBi_2Nb_{1.9}Ti_{0.1}O_9$ catalysts,[124b,135] CdS and WO_3 are synthesized from surface sulfurization of the metal core of Cd and surface oxidation of the W cluster to form a seamless contact interface between the materials.

The core–shell CdS@Au/TiO_2 structure with an electron transfer mediator (i.e., Au) exhibits high activity owing to stepwise electron transfer driven by two-step excitation of TiO_2 and CdS.[12a] Following this work, a series of composites including CdS@Au/TiO_2,[136] CdS@Au/N-TiO_2[137] and CdS@M/TiO_2 (M = Au, Ag, Pt, Pd),[138] CdS@Au/TNF (TiO_2 nanofibers),[139] and CdS@Au/$TiO_{1.96}C_{0.04}$[140] have been developed. The module (Figure 4c1) increases charge separation and prolongs electron–hole lifetimes. The incorporated porous CdS@Au/N-TiO_2 contributes to a H_2 evolution rate of approximately 9.2 μmol h^{-1}, which is approximately 270 times higher than that of Au/N-TiO_2.[137] To determine the effects of the core–shell and the role of the TiO_2 nanostructures, Au-deposited CdS/TNF and commercial TiO_2 (P25) have been examined as references.[139] The amount of H_2 produced by CdS@Au/TNF higher than that produced by CdS/TNF, CdS/Au/TNF, and CdS@Au/P25. However, these systems are not real two-photon systems, because TiO_2 only generates electrons under UV light. Biomimetic systems such as CdS@Au/$TiO_{1.96}C_{0.04}$ consisting of two visible-light components produce four times the amount of H_2 as that produced by CdS@Au/TiO_2.[140] Photoluminescence studies have revealed that the Au core captures electrons from the CB of $TiO_{1.96}C_{0.04}$ and accelerates electron transfer to the VB of CdS, which allows the electrons to be shuttled to a higher energy level, and this produces a substantial amount of H_2 on the CdS surface.

Other composites, such as CdS@Au/ZnO,[141] ZnO/CdS@Cd,[142] Cu_2O@Pt/TiO_2,[143] CdS@Pt/TiO_2,[144] Cr_2O_3@Rh/GaN:ZnO,[145] and CdS@Au/g-C_3N_4,[146] have been further examined. Pt NPs loaded ZnO/CdS@Cd exhibits a H_2 evolution rate of 1.92 μmol h^{-1}, which is 5.1 times higher than that exhibited by Pt-loaded ZnO/CdS. To understand the size effect of the core, Cr_2O_3@Rh/GaN:ZnO has been examined for water splitting.[145b] The size of the poly-protected Rh NPs can be controlled to fall within the range of 1.7 to 7.7 nm by changing the nucleation rate of the polyol synthesis. The activity of the catalyst with the smaller Rh core is higher than that with a larger Rh core. In another case, the Cu_2O@Pt/TiO_2 structure with a Pt content of approximately 0.9 wt% and a mean Pt NP size of approximately 3.1 nm has been prepared, in which the Cu_2O shell provides sites for preferential activation and conversion of CO_2 in the presence of H_2O, whereas the Pt core extracts electrons from TiO_2. The rate of formation of CH_4 is 33 μmol g^{-1} h^{-1}, which is approximately 3.0 times higher than that over Pt/TiO_2 and 3.8 times higher than that over Cu/TiO_2.[143] The conversion of CO_2 and water vapor has also been explored by using Cu_xO/Pt/N-TNT, in which TNT offers a thin wall to facilitate effective carrier transfer.[147]

3.3.1.3 *Plasmonic effect*

Interest in introducing nanoscale metals into photocatalysis comes from their light-harvesting and electromagnetic field concentrating properties induced by surface plasmon resonance (SPR), which refers to coherent oscillations of the free electrons on the metal surface against the restoring force of positive nuclei.[103a] The SPR resonant wavelength and intensity depend on size, shape, composition, and dielectric environment of the plasmon metals.[103] SPR enhances photocatalysis in three ways: by increasing light absorption, by increasing charge separation through either direct electron transfer or plasmon-induced resonance energy transfer, and by reducing charge recombination by plasmon-mediated electromagnetic field. However, it is hard to differentiate the plasmonic effects from other potential factors such as cocatalytic effect or enhanced charge separation by the metal/semiconductor junction.[148]

It has been demonstrated that Ag, Au, and Cu NPs respond to visible light by the SPR effect.[149] The compounds BiOX (X = Cl, Br) have good catalytic activities. To further improve their activities, Ag/AgCl and Ag/AgBr have been integrated with BiOCl and BiOBr. The roles of Ag in the systems have been identified by quantification experiments involving trapping of the active species and superoxide radicals.[149i] Given that the absorption edges of AgCl and BiOCl correspond to $\lambda = 382$ and 360 nm, they cannot be photoexcited under visible light, but Ag absorbs visible light owing to the SPR effect and its dipolar character. The absorbed photons generate an electron and hole, and then the electron is transferred to the CB of AgCl and further moves to the CB of BiOCl (SPR effect in Figure 4d,d1). In contrast, the absorption edges of AgBr and BiOBr are $\lambda = 490$ and 427 nm. Therefore, the electrons flow as BiOBr→Ag→AgBr in the AgBr/Ag/BiOBr structure (electron relay in Figure 4c). To take advantage of the features of both SPR and electron trapping, converting CO_2 into hydrocarbons has been conducted by using Ag, Pt, or bimetallic Ag–Pt and core–shell SiO_2@Ag NPs coupled with a TiO_2 catalyst.[149f] A selectivity for CH_4 of approximately 80% is achieved by tuning the bimetallic Ag–Pt cocatalysts. If both bimetallic catalysts and SiO_2@Ag NPs are used, the product yield is enhanced more than sevenfold over that obtained in the presence of native TiO_2.

In plasmonic Z-scheme systems (Figure 4e) such as AgCl/Ag/H_2WO_4·H_2O nanoplates,[149c] AgCl/Ag/$Bi_{20}TiO_{32}$ NCs (Figure 4e1),[149d] AgCl/Ag/Bi_2MoO_6 nanosheets,[149a] AgCl/Ag/α/β-Bi_2O_3,[149g] and AgCl/Ag/γ-TaON hollow spheres,[149h] the metal NPs serve as the electron mediator as well as the plasmonic sensitizer. Specifically, under visible-light irradiation, AgCl with a large band gap energy (E_g) of 3.25 eV cannot be photoexcited, whereas materials with relatively small band gaps (e.g., H_2WO_4·H_2O, $Bi_{20}TiO_{32}$, Bi_2MoO_6 α/β-Bi_2O_3, and γ-TaON) respond to visible light. Metallic Ag also absorbs visible light owing to the SPR effect and its dipolar character. The photoexcited electrons in the CB of a material with a small band gap combine with the holes in the highest occupied orbital of metallic Ag. The photoexcited electrons in the lowest unoccupied orbital of plasmonic Ag migrate to the CB of AgCl. Such electron transfer from Ag to the semiconductor is expected to facilitate charge transfer.

Core–shell Cu_2O@Cu NPs inside TNTs also shows a plasmonic effect (Figure 4f).[149b,e] The metal Cu core plays three roles: one, it lowers the resistance to electron transport from excited Cu_2O to the TNTs; two, it behaves as an electron storage center for charge separation; three, it enhances the photocatalytic properties of the TNTs under visible light. The maximum

amount of H_2 evolved is 45.56 μmol h^{-1}, which is approximately 12 times higher than that evolved over pure TNTs. The drawback of a bare plasmonic structure lies in fast decay of hot electrons. Their ultrafast decay across Au NPs can be overcome by coupling with CdS quantum dots (QDs) and by a Schottky junction with perovskite $SrTiO_3$ NPs (Figure 4 f1).[149e] The CdS@Au/$SrTiO_3$ catalyst shows an impressive H_2 generation rate of approximately 29.1 μmol h^{-1}, in contrast to a rate of 5.0 μmol h^{-1} offered by Au/CdS/$SrTiO_3$, on which CdS and Au NPs are individually deposited on the $SrTiO_3$ surface. These instances are consistent with the electron-relay model (Figure 4 b, c), except that the electron mediator also takes responsibility for light harvesting. Notably, both the band gap of the semiconductor and the wavelength of incident light define the role of the metal.

3.3.2. Graphene electron mediator

Graphene possesses a 2D structure, exceptional conductivity, superior mobility of charge carriers, large surface area, and excellent optical transmittance.[150] Its work function is 4.42 eV, and such a high energy level is beneficial to electron transport from the semiconductor to graphene. A series of semiconductor(s) and/or metals have been coupled with graphene to form multicomponent catalysts.[151] Although the mechanism is not fully understood, graphene in the composites is considered to promote electron shuttling from the light-absorbing semiconductor to the catalyst, to extend light absorption, and to provide a large surface area for the chemical reactions.

3.3.2.1. Semiconductor–metal composites

Since it was reported that shuttling of TiO_2 photoelectrons to spatially separated Ag nanoparticles can occur through reduced graphene oxide (RGO),[152] numerous groups have integrated semiconductors and metals with graphene. Metals in these structures behave as electron capture centers (Figure 5 a), electron relay mediators (Figure 5 b), or plasmonic components (Figure 5 c). The integration of Pt/TiO_2,[153] Pt/g-C_3N_4,[154] Pt/CdS,[155] Pt/$Sr_2Ta_2O_{7-x}N_x$,[156] Ag/ZnO NRs,[157] and Cu/TiO_2[158] on graphene has been performed, and the evolution rate increases 2–5 times relative to the rate on their counterpart references. In these cases, graphene serves to collect and transport photoinduced charges, whereas the metal particles act as an electron sink. To reveal electron transfer, three different structures, Pt/(0.5 graphene oxide (GO) + P25), (Pt/P25) + 0.5 GO, (Pt/0.5 GO) + P25, have been synthesized by different orders by using the same quantity of chloroplatinic acid.[153b] The preparation procedures influence the loading location of Pt as well as the electron-transfer routes. The (Pt/0.5GO) + P25 sample presents the highest H_2 production rate of approximately 5921.1 μmol h^{-1} g^{-1}, as graphene oxide induces irreversible electron transfer of the type P25 → GO → Pt. In the CdS/Pt/GO composite, graphene serves as an electron collector and transporter to increase charge lifetime, which leads to a H_2 production rate of 1.12 mmol h^{-1} at a graphene content of 1.0 wt% and a Pt content of 0.5 wt%.[155] The dispersion of

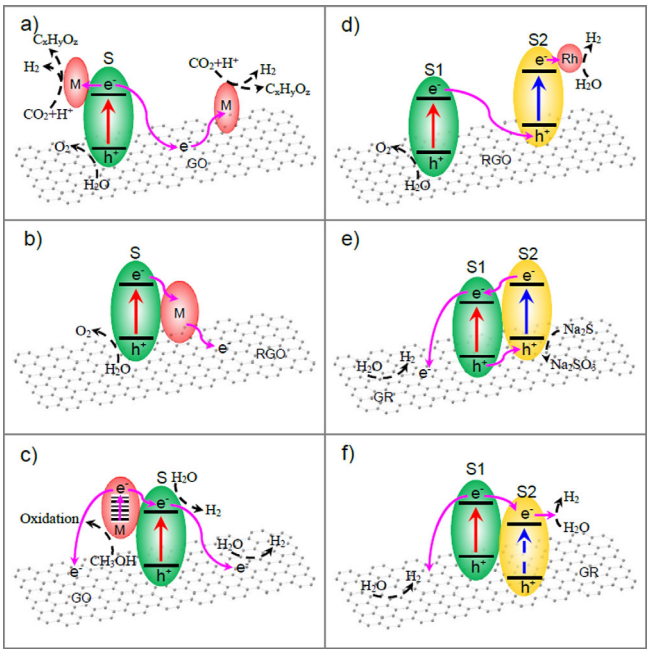

Figure 5. Charge transport in the a) semiconductor–graphene–metal electron sink system (adapted from ref. [159]), b) semiconductor–graphene–metal electron relay system (adapted from ref. [161]), and c) semiconductor–graphene–metal plasmonic effect system (adapted from ref. [163]). Charge transport in the d) semiconductor–graphene–semiconductor system (adapted from ref. [12b]), e, f) semiconductor junction–graphene systems (adapted from ref. [178] and [180]).

a noble metal[159] or bimetal[160] on the semiconductor–graphene composite also improves CO_2 conversion. Reducing metal ions (e.g., $PtCl_6^{2-}$, Pd^{2+}, Ag^+, and $AuCl_4^-$) is a simple polyol process to load metal (e.g., Pt, Pd, Ag and Au) nanoparticles on reduced graphene oxide/TiO_2. A 2.0 wt% Pt-doped composite shows the best activity; it achieves a total CH_4 yield of 1.70 μmol g_{cat}^{-1}.[159] The Pt NPs play a critical role in trapping electrons over both the TiO_2/Pt and GO/Pt interfaces (Figure 5 a).

Metal nanoparticles are believed to functionalize as electron relay mediators in graphene-supported Ag_3PO_4/Ag/AgBr[161] and graphene oxide/Ag/AgCl composites (Figure 5 b).[162] Ag_3PO_4 is one of only a few materials that exhibits excellent oxidative capability for O_2 evolution from water. The graphene-supported Ag_3PO_4/Ag/AgBr catalyst can be prepared by the photoassisted deposition–precipitation method.[161] The composite exhibits an O_2 evolution yield (76 μmol h^{-1}) that is approximately 1.3 times higher than exhibited by Ag_3PO_4/Ag/AgBr (48 μmol h^{-1}) and a yield that is approximately 2 times higher than that offered by pristine Ag_3PO_4 (38 μmol h^{-1}). The improved yield is attributed to CB depletion of Ag_3PO_4 caused by additional Ag/AgBr. This composite leads to a long lifetime of the photogenerated holes and a downward shift in the VB of Ag_3PO_4 owing to charge transfer to Ag and subsequently to RGO. In the graphene oxide/Ag/AgCl composite, in which GO and AgCl act as activated photocatalysts, metallic Ag shuttles the electrons from AgCl to GO.[162] The electron–hole pairs of a low energy level recombine in space through Ag as a solid-

state electron mediator, and the remaining charge carriers have a high energy level for redox reactions.

Graphene and RGO have also been used as supports for plasmonic catalysts, such as in Au/TiO_2/graphene,[163] Ag/TiO_2/graphene,[164] Au/N-$La_2Ti_2O_7$/RGO,[165] Ag/Ag_2CO_3/RGO,[166] and graphene sheet grafted AgCl@Ag.[167] In these cases, metal NPs are photoexcited under visible-light irradiation owing to plasmonic resonance. Charge separation is accomplished by transferring the photoexcited electrons from the metal NPs to the semiconductors. The electrons then flow into the graphene sheets in the graphene–semiconductor system (Figure 5c). Both the graphene surface and the CB of the semiconductor function as active sites for H_2 production. Such a scenario retards the recombination of electron–hole pairs and suppresses the reverse reaction by separating the redox sites. For instance, graphene-based Au-TiO_2 catalysts have been prepared with Au/TiO_2-GO composite weight ratios of 0, 0.05, 0.10, 0.25, and 0.50%.[163] In the system, the H_2 evolution rate increases to 296 $\mu m\,h^{-1}\,g^{-1}$ as the Au concentration increases up to 0.25%, but an excess amount of Au NPs may act as a recombination center, which is evidenced by the lower H_2 evolution rate of approximately 197 $\mu m\,h^{-1}\,g^{-1}$ for the 0.5% sample.

3.3.2.2. *Semiconductor–graphene composites*

To prove the role of graphene as a support and relay material between different light absorbers (Figure 5d), the anatase/graphene/rutile,[168] $BiVO_4$/graphene/(Ru/$SrTiO_3$:Rh),[12b,169] metal sulfide/RGO/TiO_2,[170] ZnO/RGO/CdS,[171] and $Fe_2V_4O_{13}$/RGO/CdS[172] catalysts have been studied. In these structures, photoexcited electrons of the n-type semiconductor are transferred to another catalyst through RGO to achieve water splitting or CO_2 reduction. The interface between the different materials is the most active part for the reactions. Fast charge migration at the interface provides a huge amount of reaction opportunities for photoinduced carriers, as RGO is used as an electron mediator between Ru/$SrTiO_3$:Rh (H_2) and $BiVO_4$ (O_2).[12b] The electrons of $BiVO_4$ are transferred to the vacancies in the impurity levels of Ru/$SrTiO_3$ by RGO. The electrons in Ru/$SrTiO_3$:Rh reduce water to H_2 on the Ru cocatalyst, whereas the holes left on $BiVO_4$ oxidize water to O_2. The key factor that enables efficient electron transfer relies on a balance between the degree of GO reduction and the level of hydrophobicity. For the case in which RGO works as a carrier transport channel, the ZnO NR/RGO/CdS catalyst exhibits a H_2 generation rate (0.6 $mmol\,h^{-1}$) that is 3.8 times higher than of the CdS/ZnO reference. The optimal contents of the RGO nanosheets and CdS NPs are 2 wt% and 20 at%.[171a] An example for CO_2 reduction is a system consisting of $Fe_2V_4O_{13}$ nanoribbon/RGO/CdS NPs grown on a stainless-steel mesh scaffold.[172] The holes stored by CdS oxidize H_2O to O_2, whereas the electrons stored by $Fe_2V_4O_{13}$ reduce CO_2 to CH_4. As a result, the combination of CdS and $Fe_2V_4O_{13}$ increases the CH_4 evolution rate to a value threefold higher than that of the $Fe_2V_4O_{13}$ nanoribbons, and the activity of the RGO system further increases to approximately 2.10 $\mu mol\,g^{-1}\,h^{-1}$.

A variety of noble-metal-free cocatalysts have been integrated with graphene–semiconductor composites, such as MoS_2,[173] $Co_{0.85}Se$,[174] NiO_x,[175] $Ni(OH)_2$,[176] and RuO_2.[177] In these materials, not only are the electron–hole pairs separated but there are more sites available for reduction. The MoS_2/graphene/TiO_2 composite reaches a H_2 production rate of 165.3 $\mu mol\,h^{-1}$ when the MoS_2/graphene cocatalyst content is 0.5 wt% and the graphene content in this cocatalyst is 5.0 wt%.[173a] The electrons in TiO_2 are transferred to the MoS_2 nanosheets through the graphene sheets and they then react with adsorbed H^+ ions at the edges of MoS_2 to form H_2. Moreover, the electrons are transferred to the MoS_2 nanosheets on the surface of TiO_2 or to the C atoms on the graphene sheets where they can react with H^+ to produce H_2 (similar to Figure 5a). Metal oxides are rarely used in pure form for CO_2 reduction, whereas Ni/NiO(NiO_x) has been identified as an effective cocatalyst. Different amounts of graphene (0–5 wt%) in the NiO_x/Ta_2O_5/RGO catalyst have been tested for the conversion of CO_2 in solution into CH_3OH and H_2.[175] The catalyst containing 1% graphene displays the highest conversion rate of CO_2 to CH_3OH, and it produces 3.4 times more CH_3OH ($\approx$0.82 $\mu mol\,h^{-1}$) than the corresponding catalyst without graphene. However, improper loading of graphene on the samples is detrimental, and this is ascribed to a trade-off between its high charge-transfer capability and its shielding effect on light absorption.

Materials with semiconductor junctions coupled to GO have been constructed, as in Figure 5e.[178] The CdS@TaON/GO catalyst shows a stable H_2 production rate of 633 $\mu mol\,h^{-1}$ at a GO content of 1 wt% and a Pt content of 0.4 wt%; this rate is approximately 141 times higher than that shown by pristine TaON. The presence of CdS@TaON reduces electron recombination, and GO serves as an electron acceptor and transporter to increase the lifetimes of the charges. In the CdS/graphene/$ZnIn_2S_4$ porous architecture, the 3 wt% CdS QD decorated architecture containing 0.4 wt% Pt shows a H_2 production rate of 1.9 $mmol\,h^{-1}$, which is approximately 2.7 times higher than that produced over $ZnIn_2S_4$.[179] The rate is further increased to 2.7 $mmol\,h^{-1}$ if the composite is coupled with 1 wt% graphene. Injection junctions with graphene composites have also been developed, as in the CuO/TiO_2/graphene,[180] CdS/TiO_2/graphene,[181] hierarchical CdS/1D ZnO/2D graphene,[182] and NiS/$Zn_xCd_{1-x}S$/RGO composites. For CuO/TiO_2/graphene, the rational addition of Cu or graphene improves the activity of TiO_2.[180] The maximum H_2 evolution rate is 2905.0 $\mu mol\,g^{-1}\,h^{-1}$. The electrons of TiO_2 are injected into graphene or CuO through a percolation mechanism (Figure 5f), at which they then react with H^+ or H_2O that is adsorbed on the surface of graphene or Cu. In contrast, in the NiS/$Zn_xCd_{1-x}S$/RGO composite, NiS is functionalized as an oxidation-active site to assemble photogenerated holes. RGO serves as an electron collector and transporter and provides reduction active sites for H_2 production.[183] The catalyst achieves a high H_2 production rate of 375.7 $\mu mol\,h^{-1}$ and an apparent quantum yield of 31.1% at $\lambda =$ 420 nm.

3.4. Two/multiphoton electrodes (photoelectrochemical systems)

Basic PEs are fabricated from a single p-type or n-type semiconductor or from two or more semiconductors. Single-semiconductor electrodes require a band gap of at least approximately 2.3 eV to generate the necessary voltage to split water, which leads to a maximum solar-to-fuel (STF) efficiency of 7%.[184] To prepare more efficient PEs, a two/multiphoton scheme is desirable owing to optimal integration of narrow-band-gap semiconductors, which in turn allows a wide solar spectrum to be absorbed for high photovoltage.[4b,185] Two/multiphoton electrodes can be built through various strategies such as semiconductor composites, QD sensitization, and plasmonic doping.

3.4.1. Semiconductor–hybrid electrodes

3.4.1.1. Heterojunction electrodes

The p–n junction separates charges by an internal electric field induced by band bending. A p-$CaFe_2O_4$/n-TaON anode has been fabricated on fluorine-doped tin oxide (FTO) glass by electrophoretic deposition of two semiconductors.[186] Upon irradiating light from the backside of the FTO glass, TaON absorbs partial light and carriers are generated. $CaFe_2O_4$ absorbs the remaining light that also excites electrons. The electrons from $CaFe_2O_4$ (S2) move toward the substrate through n-TaON (S1), and holes from TaON migrate to the surface of $CaFe_2O_4$ by a potential difference (Figure 6a). Thus, the anode absorbs high-energy light to excite efficient charge separations for water oxidation. The introduction of the $CaFe_2O_4$ overlayer on the TaON electrode increases the photocurrent density approximately fivefold. To improve stability, an ultrathin carbon sheath is coated on a p-Cu_2O/n-TaON NR array photoanode as a surface protection layer. The passivated anode exhibits an incident photon-to-current efficiency (IPCE) of 59% at $\lambda =$ 400 nm, shows a photocurrent of 3.06 mA cm^{-2}, and retains approximately 87% of the initial activity after irradiation for 1 h. Not only is the onset potential negatively shifted but the photocurrent density and photostability are also improved relative to the unpassivated anode.[187] These improvements are due to fast transfer of electrons together with high conductivity and shielding from the electrolyte by the carbon jacket. In addition to the surface catalytic effect, bulk charge separation is achieved through introducing discrete p-Co_3O_4 nanoislands onto n-$BiVO_4$. The anode offers a photocurrent of 2.71 mA cm^{-2} at 1.23 V, with a photoconversion efficiency of 0.659%.[188] The p–n junction has also been introduced in Si/TiO_2/Pt photocathodes for CO_2 reduction.[189] The results show good performance for the formation of methanol (0.88 mmol L^{-1}), ethanol (2.60 mmol L^{-1}), and acetone (0.049 mmol L^{-1}), presenting faradaic efficiency of 96%.

Integration of two n-type semiconductors is an alternative approach. The most studied materials are TiO_2, WO_3, α-Fe_2O_3, g-C_3N_4, and $BiVO_4$. TiO_2/$ZnIn_2S_4$,[190] N-TNT/TaO_xN_y (N-TNT = N-doped TiO_2 nanotube),[191] WO_3/$BiVO_4$,[192] coupling Fe_2O_3 with $MgFe_2O_4$,[193] and $ZnFe_2O_4$,[194] 3D CoO_x/C_3N_4/Ba-TaON,[195] and CoO_x/C_3N_4/WO_3[196] have been explored for PEC water splitting. By coupling N-doped TNTs with a thin TaO_xN_y layer, both charge-generation materials are separated at their interface owing to a potential gradient. The thin TaO_xN_y film serves as a passivation layer that reduces the surface-trap sites of N-TNT.[191] This complementary factor results in a high photocurrent and improves visible activities by approximately 3.6 times over that of the N-TNT electrode. WO_3 is an indirect band-gap semiconductor ($\approx$2.6 eV) with a very low absorption coefficient, approximately 12% of the solar spectrum. To improve the performance, WO_3/$BiVO_4$ nanowires (NWs) have been grown on FTO, in which $BiVO_4$ is a primary light absorber and WO_3 acts as an electron conductor. The IPCE value of the nanowire is 31% at $\lambda =$ 420 nm, whereas that of the planar WO_3/$BiVO_4$ films is 9.3%.[192a] The NW anode produces a photocurrent of 3.1 mA cm^{-2} and an IPCE of approximately 60% at $\lambda =$ 300–450 nm for water oxidation.[192c] In photoanode-driven CO_2 reduction, the Co-Ci/$BiVO_4$/WO_3 photoanode with a Cu cathode system shows a stable photocurrent and 51.9% faradaic efficiency for CO and C_1–C_2 hydrocarbons.[192b]

Hematite is an earth-abundant material that has a favorable band gap of 2.1 eV. Its performance is restricted by poor kinetics for water oxidation and short hole diffusion lengths (2–4 nm).[4b,197] To compensate these shortcomings, branched Co-Fe_2O_3 NR/$MgFe_2O_4$ has been devised as a photoanode. Driven

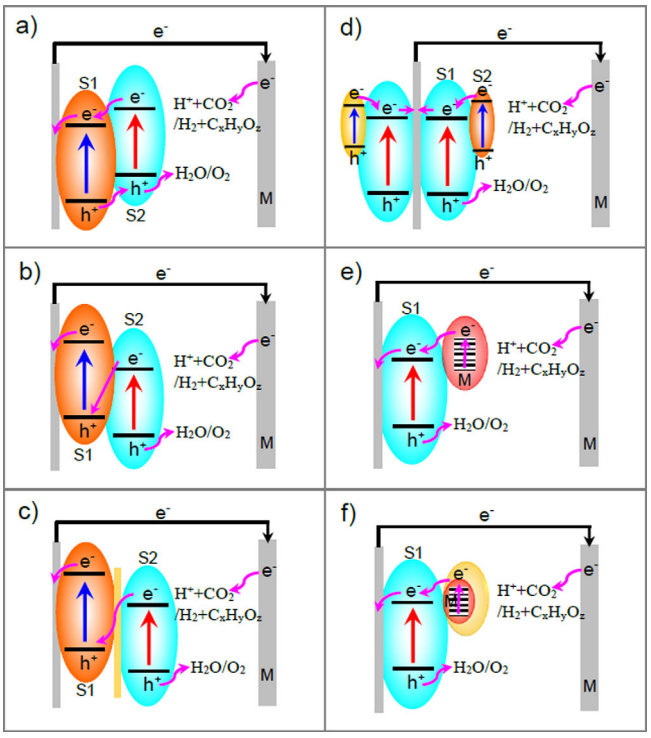

Figure 6. Charge transport at a) heterojunction photoanode (adapted from ref. [186]) and b) tunnel junction photoanode (adapted from ref. [200a]). c) Tunnel junction photoelectrode through a thin insulating layer (adapted from ref. [198]). d) Charge transport at dual-sided quantum dot cosensitized photoanode (adapted from ref. [219]). Charge transport at semiconducting photoanodes with e) a metal nanostructure or f) a core–shell metal insulator nanostructure (adapted from refs. [220e], [223b]).

by band alignment, the electrons migrate from the CB of $MgFe_2O_4$ to that of the Co-Fe_2O_3 NRs, from which they are then transported to the Ti substrate along the Co-Fe_2O_3 NRs. The holes in the VB of the impurity level of Co-Fe_2O_3 are transferred to the VB of the impurity level of $MgFe_2O_4$. As a result, the anode presents a photocurrent density of approximately 3.34 mA cm^{-2}, which is 2.69, 1.95, and 1.78 times higher than that of Fe_2O_3NR, Co-Fe_2O_3NR, and 1 D Co-Fe_2O_3NR/$MgFe_2O_4$.[193] Relative to metal oxides, g-C_3N_4 has attracted much interest in response to visible light. The branched CoO_x/C_3N_4/WO_3 anode exhibits a photocurrent density of 3.61 mA cm^{-2}, which is approximately 1.31 times greater than that of WO_3/C_3N_4 nanosheets.[196] In this architecture, WO_3 is an electron acceptor, and CoO_x functions as a surface oxidation catalyst.

3.4.1.2. *Tunnel junction electrodes*

A tunnel junction is a thin insulating layer or electric potential between light absorbers. Charge carriers can pass through the barrier by quantum tunneling.[198] In tunnel-junction electrodes, a redox reaction occurs at the interface of the semiconductor–electrolyte. The junction interface serves as a site for the recombination of the majority of carriers (Figure 6 b). There are two possibilities for charge transport from one absorber to another. In the first case, the semiconductor has different band-bending properties near the junction. A potential energy barrier across the interface blocks a minor amount of the carrier flow but permits the majority of flow towards the junction. This situation has been realized in n-TiO_2/n-Si NW,[199] n-Fe_2O_3/p- or n-Si NW[200] anode, and InGaN/GaN/Si cathode.[201] In these cases, charge carrier flow is enabled if the two semiconducting absorbers are photoexcited in a synergistic manner. The VB of the top absorber is lower than that of the underlying absorber, and holes from S1 are transported by tunneling to combine with the electrons on the CB of S2 through an extremely thin depletion layer. For instance, Si NWs absorb photons (600 nm $< \lambda <$ 1100 nm) that are transparent to hematite ($\lambda =$ 300–580 nm) and convert the energy into additional photovoltage.[200] Band alignment at the junction reflects holes back into hematite, which helps to reduce the loss of holes. Notably, without the highly doped layers, an inadvertent p–n junction would form at the interface.[184,202] This would drive electrons and holes in the wrong directions and would cause recombination of minority carriers and reduce fuel-generation efficiencies. Alternatively, a passive or protection layer with a VB below that of the absorber allows a hole to tunnel through the thin layer or to be transported through a defect band in the layer (Figure 6 c).[198] The former scheme has been realized with thin layers of TiO_2 grown on n-Si or p-Cu_2O[14,203] or with a thin epitaxial layer of $SrTiO_3$ grown on Si(0 0 1).[204] However, the thickness of the layer needs to be controlled, as tunneling introduces a large series resistance for films thicker than a few nanometers. The latter scheme has been achieved by using amorphous TiO_2 layers coated with a number of absorbers: n-Si, n-GaAs, and n-GaP.[205] The protection layer can be as thick as 140 nm, which rules out any tunneling effect. A thin TiO_2 interlayer (4–25 nm) is required in a dual absorber of a $BiVO_4$ (S2) and Si (S1) anode to realize an increase in the photocurrent and a shift in the onset potential. The anode shows 1.0 mA cm^{-2} at 1.23 V with an onset potential of 0.11 V; thus, there is a 3.3-fold enhancement in current density and the onset potential is shifted in the negative direction by 300 mV relative to that of the $BiVO_4$/FTO photoanode.[206] A further increase in the water splitting activity can be expected by improving the interlayer conditions and by loading proper co-catalysts.

3.4.2. *Quantum-dot-sensitized electrodes*

Integrating quantum dots with bulk or nanostructured semiconductors increases the light absorbance of PEs. Thus, CdS[207] and CdSe[208] have been adopted as sensitizers on TiO_2 nanostructures for photosynthesis. The cascade structures of CdSe/CdS,[209] PEDOT/CdSe/CdS,[210] and ZnS/CdSe/CdS[211] on TiO_2 PEs exhibit more enhancement in the current response than the single-sensitized PEs. The maximum photocurrent achieved by the CdSe/CdS/TiO_2 PE is 14.9 mA cm^{-2}, which is three times that of the CdS/TiO_2 and CdSe/TiO_2 PEs. If CdS and CdSe are inversely deposited on a TiO_2 film to form a CdS/CdSe/TiO_2 structure, the current density is much lower than that of the CdSe/CdS/TiO_2 electrode.[209] This is ascribed to the fact that the alignment of the Fermi levels between CdSe and CdS induces upward and downward shifts in the band edges. The energy potential levels of intermediate CdSe are higher than those of CdS, which results in a notable barrier for the injection of electrons from the outer CdS layer and the transfer of holes out of the inner CdSe layer.

Branched CdS/TiO_2/SnO_2 NRs have been studied to understand band alignment of multiple structures in the parent semiconductors.[212] The PE induces a photocurrent density of 8.75 mA cm^{-2} at zero bias, which is more than four times higher than that of the SnO_2/TiO_2 electrode. To verify the morphology effect of the sensitizer, a series of CdS, CdSe, and CdSeS NRs deposited onto TiO_2 NW PEs have been explored.[208b] If the sensitizer is changed from a particle to a rod to a stump-shaped morphology, the latter two anodes have higher photocurrent densities, which comes from competition between light absorption, recombination loss, and surface area. The CdSe/TiO_2-NW electrode presents the highest initial photocurrent owing to the smallest band gap. The CdS/TiO_2-NW anode exhibits the lowest photocurrent with the highest electron injection efficiency. The CdSeS/TiO_2-NW heterostructure is a favorable one in terms of the level of the photocurrent and stability.

The cascade concept has been transplanted to extend the absorption spectrum in ZnO-based PEs, such as in IrO_x·n H_2O-modified CdSe/CdS/ZnO NWs,[213] CdSe/CdS/ZnO NRs,[214] $ZnIn_2S_4$/ZnS/ZnO nanotube arrays,[215] NiO/CdS@ZnO composites,[216] ZnSe/CdS/CdSe/ZnO NWs,[217] CdSe/CdS/ZnO/WO_x hierarchical NWs,[218] and double-sided CdS/ZnO|ZnO/CdSe NWs.[219] Triple-sensitized ZnO NWs can be fabricated on FTO through a facile hydrothermal and anion-exchange reaction, followed by a chemical bath deposition approach.[217] Through synergistic light absorption and multigraded band-gap levels

between the materials, the PE delivers a photocurrent intensity of 5.3 mA cm^{-2}, which exceeds that of a single- or co-sensitized PE and is approximately 11 times higher than that of bare ZnO NWs. Although the electrons of CdSe are transferred to ZnO through the CdS layer, the presence of this intermediate layer in CdSe/CdS/ZnO increases charge recombination and limits the efficiency of photoelectron collection. To overcome these drawbacks, rational separation of CdS and CdSe on each side of ZnO in a dual-sided PE is a wise tactic (Figure 6d).[219] The Fermi levels of CdS, CdSe, and ZnO are aligned so that the CBs of CdS and CdSe are close enough to allow delocalization and transfer of the photoelectrons. The anode shows high activity for water oxidation with a photocurrent density of 12 mA cm^{-2}.

3.4.3. Plasmonic electrodes

Plasmonic effects have led to compelling evidence for water splitting. The PEs affected by metal NPs can be divided into those with direct contact to the semiconductor (Figure 6e) and those separated from the semiconductor by an insulating spacer (Figure 6f). As a light absorber, Au has been used to sensitize TiO_2 PEs to generate additional charge carriers for water oxidation.[220] This is due to amplification of the electric field near the semiconductor surface induced be SPR; this increases the photon absorption rate of TiO_2 and improves the photoactivity.[221] Au NPs assembled with a TiO_2-based photonic crystal substrate can achieve a photocurrent density of approximately 150 μA cm^{-2}. Matching the SPR wavelength to the photonic band gap of TiO_2 boosts hot electron injection and thus enhances activity.[220e,222] By manipulating the shape of the decorated Au structures, a mixture of Au NPs and NRs deposited on TiO_2 NWs shows water oxidation over the entire UV/Vis region ($\lambda \approx 300$–800 nm).[220b] A nanobamboo array with various metal-semiconductor segments (ZnS-Ag-CdS-Au-CdSe) has also been designed to improve charge transfer.[220c] The surface of each segment is in direct contact with the electrolyte, and the holes easily migrate to the semiconductor/electrolyte interface because of a shorter transfer distance in the radial direction. As a result, the architecture facilitates interfacial charge transfer and accelerates photocatalytic transformations.

Direct exposure of plasmonic metals to the electrolyte leads to their corrosion and dissolution. One attempt to address this problem relies on coating the metals with a protecting layer.[220d] Plasmonic Ag shows great potential for redox applications.[220c,223] By loading core–shell $Ag_3(PO_4)_{1-x}$@Ag onto ZnO NRs (Figure 6f), water oxidation activity can be achieved with a maximum photocurrent of 3.1 mA cm^{-2} and an IPCE of 60% at $\lambda = 400$ nm.[223b] The SPR of Ag increases the optical absorption and the rate of electron–hole formation near the $Ag_3(PO_4)_{1-x}$/ZnO junction. Another strategy is to embed plasmonic metals into the semiconductor photocatalyst,[220g,224] as gold NPs sandwiched between TiO_2 NRs and a CdS layer play a dual role in enhancing the efficiency.[220g] The Au NPs first serve as an electron relay that facilitates charge transfer between CdS and TiO_2 if the QDs are photoexcited by wavelengths shorter than 525 nm. Second, the Au NPs act as a plasmonic sensitizer, which enables the conversion at wavelengths longer than the band edge of CdS, and this extends the wavelength from 525 to 725 nm. The dual role of Au leads to a photocurrent of 4.07 mA cm^{-2} under full solar spectrum irradiation and a maximum STF of 2.8%. An alternative method is to utilize layered core–shell structures, such as uniform and tapered Si@Ag NWs,[225] which combine the geometry of the NWs with the SPR in the metal core to confine light within a thin semiconductor shell. To obtain cost-effective and scalable plasmonic light harvesting, core–multishell Fe_2O_3@Al@Si NW structures with Al thin films as the intermediate shell have been developed with photocurrent densities comparable to those of Fe_2O_3@Ag@Si NWs.[226] A PE with a dual absorber system consisting of Si and hematite reaches a photocurrent density of approximately 11.81 mA cm^{-2}, which corresponds to a STF efficiency of 14.5%.

Developing PEs with charge carriers purely generated by SPR is another promising approach.[227] One realization of such PEs is based on Au nanostructures. Au NRs are grown by electrodeposition on a porous aluminum oxide template, which is then coated with a thin TiO_2 layer for charge separation. To build an autonomous unit, tiny Pt NPs are loaded to trigger the reduction of H^+ after capturing the hot electrons. A cobalt cocatalyst is additionally loaded to feed the metal back with electrons. This all-in-one unit is thus built and produces H_2 at a rate of 5×10^{13} molecules cm^{-2} s^{-1} under 1 sun illumination.[227a] Au NRs capped with TiO_2 can also be used as an effective photoanode to collect and conduct hot electrons to the platinum electrode at which H_2 gas evolves.[227b] The resultant positive charges in the Au NRs function as holes and are extracted by OEC to produce O_2 gas. The anode shows enhanced responsivity across the plasmon band, as evidenced by fuel production efficiencies that are up to 20 times higher at visible wavelengths than at ultraviolet wavelengths.

3.5. Two-photon cells (photoelectrochemical systems)

PEC performance has been explored extensively at the electrode level, whereas cell design has received less attention.[4b,19a,b,228] It is convenient to assemble two or more light absorbers in a complete cell. Various techniques have been developed at the cell level to trade-off between light absorption and reaction potentials, such as PV-PEC cells, Z-scheme cells, PEC diodes, and all-in-one membranes. These cells consist of two electrodes, one or both of which is photoactive. Semiconductors in the cells are used either to create PV junctions or as PEs. The photoanode and cathode can be physically separated in a wired configuration or combined into a monolithic structure.[229]

3.5.1. Wired cells

3.5.1.1. PV-PEC cells

In single-photon cells, a semiconductor material is used as either the photoanode or the cathode with a counter electrode. At the electrolyte/semiconductor interface, charge carriers are separated and all important redox reactions occur. This

solid/liquid junction suffers from recombination and results in a low photovoltage. A PV junction can be introduced into a PEC device to generate an additional bias to assist charge separation.[229,230] PV-PEC devices (Figure 7a) include a bottom PV and a semiconductor/electrolyte junction. This stacked structure involves the arrangement of two absorbers that need optimum energy combinations in the ranges of 0.95 to 1.20 and 1.60 to 1.80 eV.[231] The classic PV materials GaAs and $GaInP_2$ are good candidates that can be used to enable such an adaptation owing to their adjustable optoelectronic properties. A typical cell is an assembly of a GaAs p–n bottom cell and a $GaInP_2$ top cell with a Pt foil as the counter electrode. The top $GaInP_2$ layer (≈1.83 eV) is designed to absorb more energetic photons, which leads to a high photovoltage. The bottom p–n junction (≈1.42 eV) absorbs less energetic photons and generates an additional photovoltage.[232] One set of electrons and holes are recombined at the tunnel junction. The resultant photovoltage is greater than the required potential for photoelectrolysis, and this drives the water reductive reaction at the semiconductor electrode. The H_2 production efficiency of the cell reaches 12.4%. Conditioning the absorber interface further with RuO_2 increases the potential of the device with a STF efficiency of approximately 14%.[232a] However, the

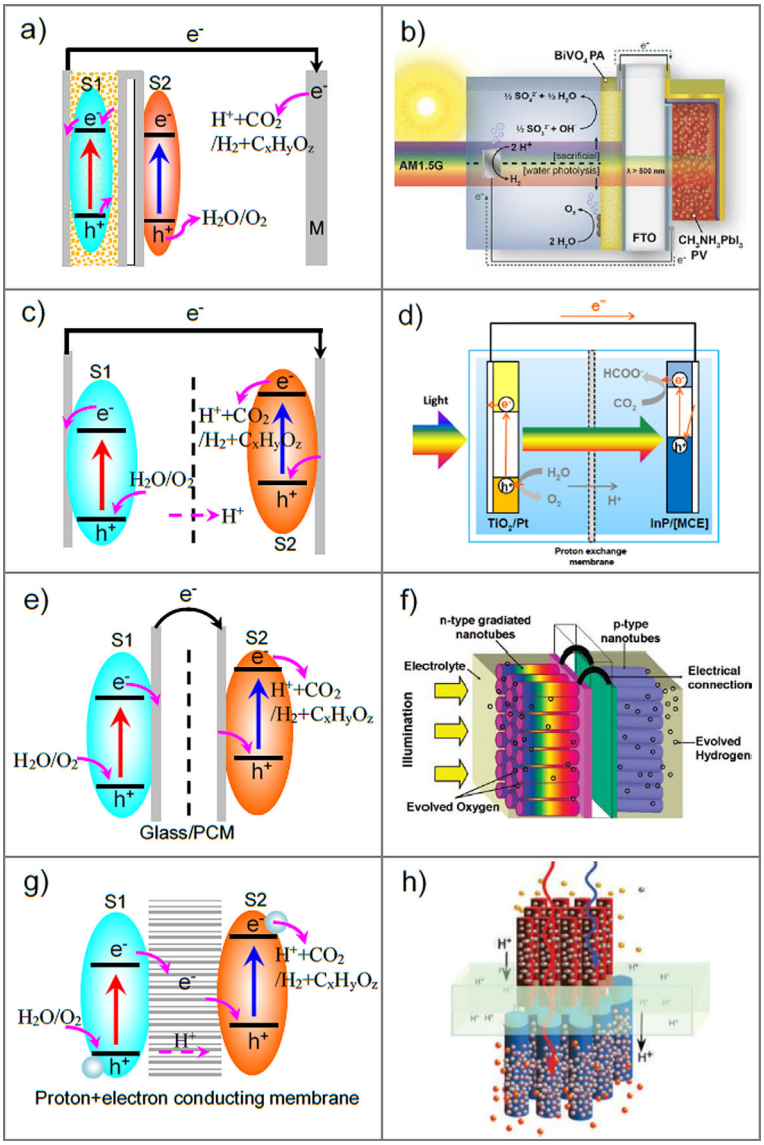

Figure 7. a) PV-PEC cell and b) example of a tandem $BiVO_4$-$CH_3NH_3PbI_3$ device for solar fuels generation (reprinted with permission from ref. [238a], copyright 2015 American Chemical Society). c) Z-Scheme PEC cell and its example d) with a two-electrode configuration comprising translucent Pt-loaded TiO_2 and [MCE2A + MCE4]-modified InP (reprinted with permission from ref. [251], copyright 2011 American Chemical Society). e) PEC diode and the example of f) a self-biased diode consisting of an n-type compositionally graded nanotube photoanode and a p-type nanotube cathode (reprinted with permission from ref. [253g], copyright 2009 American Chemical Society). g) All-in-one membrane and its example h) the blue portion of sunlight is absorbed by the semiconductor oxide photoanode (red color), at which water is oxidized to release protons. The red portion of light passing through is absorbed by the Si nanorod photocathode (blue color), which drives the protons and electrons to produce hydrogen. The membrane is permeable to the generated protons and conduct electrons between the electrodes (reprinted from ref. [262], copyright 2009 Nature Publishing Group).

use of expensive and scarce light-absorbing materials limits practical application of this device.

In the search for low-costing materials, various devices have been built with silicon materials.[15,233] The combination of a W-$BiVO_4$ photoanode with a double-junction silicon (a-Si:H/nc-Si:H) PV device offers a benchmark efficiency of 5.2%.[233e] In this cell, photons are filtered by the front $BiVO_4$ anode, at which a gradient W-doping profile is introduced to enhance charge separation. Then, the remaining photons are absorbed by the PV structure. A junction cathode has also been made from hydrogenated amorphous and microcrystalline silicon (a-Si:H/μc-Si:H).[233a,b] Such a system has the added advantage of absorbing sunlight at different wavelengths. By adjusting the photocurrent of the structure, the maximum STF efficiency reaches up to 13.26%.[233f] Another method is to introduce an external bias through the PV cells. By connecting the OEC to the p-type terminal and the HEC to the n-type terminal of the PV module, the voltage and current of the system are constrained to the same value, that is, they are equal. In this case, the STF efficiency can reach >10% by a series interconnected PV module (c-Si or CIGS).[234]

A series of dye-sensitized solar cell (DSC)-PEC cells have also been fabricated by Grätzel et al,[235] Mora-Seró et al,[236] and Park[237] et al. In these devices, the PE functions as a light absorber, and typical materials include WO_3, Fe_2O_3, and CdS/TiO_2. Incident light beams are transmitted from the photoanode to the underlying DSCs. In DSCs, wide-band-gap semiconductors are combined with visible-light-absorbing dyes. The photoanode and the DSCs are complementarily designed to exploit a substantial part of the solar spectrum. The STF efficiencies are 1.17 (Fe_2O_3/DSC) and 3.10% (WO_3/DSC). Recently, water-splitting assemblies composed of a photoelectrode (e.g., $BiVO_4$, Fe_2O_3, TiO_2, and Cu_2O) and a $CH_3NH_3PbI_3$ perovskite solar cell have been developed.[238] The tandem configuration (Figure 7b) allows efficient photon management with the photoelectrode harvesting visible light and the underlying solar cell capturing lower energy visible–infrared wavelengths in a single-pass excitation; this results in a STF efficiency of 2.5%.[238a] Moreover, the PV module might even be the sole supplier of the bias; for example, two perovskite solar cells connected in series serve as an external power source for photolysis with a STF efficiency of 12.3%.[239] However, because of the presence of hygroscopic amine salts and the distorted crystal structure, perovskites are susceptible to light, temperature, and aqueous environments, which not only restrict their long-term stability but also weaken their direct use as photoanodes.[240]

3.5.1.2. *Z-scheme cells*

Given that water splitting entails two half-reactions, it seems natural to use two light absorbers in a two-PE system in which the photocathode and photoanode are connected in series. The redox reaction is separated into two half-reactions (Z-scheme cell in Figure 7c).[241] The majority of carriers recombine at the photocathode/anode interface, whereas a minority of carriers in the two semiconductors move towards the semiconductor/electrolyte interface to carry out the individual half-reactions. The better options for the anode and cathode are n-type and p-type materials. Such a combination of two band gaps produces a wide electrochemical window. Relative to PV-PEC cells, this cell offers advantages including a simple fabrication process, a low operation voltage, and relatively high efficiency. However, one-electron transfer in this system requires the absorption of two photons.

A Z-scheme cell with carbon-doped TNTs ($TiO_{2-x}C_x$) as the anode (S1) and Pt NPs incorporated in TNTs as the cathode (S2) delivers a photocurrent of approximately 2.5–2.8 mA cm^{-2} and can run continuously for approximately 80 h for visible-light water splitting.[242] Following this route, various Z-scheme cells have been built, such as n-TiO_2 NRs/FTO (S1) and C/p-Cu_2O NWs/Cu (S2),[243] Fe_2O_3NR and p-$GaInP_2$,[244] NiO/TiO_2NW and Pt NP/Si NW,[245] TiO_2/indium tin oxide (ITO) and Bi-$O_{1-x}Cl_{1-y}$/ITO,[246] ZnS/CdS/TiO_2/TCO and MoS_2/CdS/TiO_2/TCO,[247] CdS/TiO_2 NRs and CdSe/NiO,[241b] and $BiVO_4$ and Cu_2O.[248] The cells normally exhibit STF efficiencies in the range of approximately 0.1% or less. A self-driven cell with CdS/TiO_2 NR as the anode and CdSe/NiO as the cathode shows a maximum efficiency of 0.17% for overall water splitting. Average gas evolution rates of 2.24 (H_2) and 1.07 (O_2) μmol h^{-1} cm^{-2} are achieved with approximately 95% faradic efficiency.[241b] A higher STF efficiency of approximately 0.91% is obtained by using a hematite anode and an amorphous Si cathode with $NiFeO_x$ and Pt/TiO_2 overlayers.[249] Recently, a dual PE device consisting of a metal nitride NW anode and a Si/InGaN NW cathode has been reported to provide a power conversion efficiency of 2%.[241a] Pairing the PE with a PV as Z-scheme electrodes further improves the configuration. Overall water splitting with a STF efficiency of approximately 2.5% is achieved by a device consisting of an anode (FeOOH/Mo:$BiVO_4$/FTO) and a Ni/Si-cell/FTO cathode.[250]

Reduction of CO_2 to formate by using H_2O as an electron donor and a proton source has been realized in a Z-scheme device (Figure 7d).[251] In this device, the conjugating p-type InP/Ru complex polymer and TiO_2/Pt are used as the working and counter electrodes. The selectivity for formate production is above 70%, and the STF efficiency is 0.03–0.04%. However, reduction of CO_2 by using a p-type semiconductor requires a large bias potential, as the VB potentials of these semiconductor are not positive enough to oxidize water.[251] Some n-type semiconductors are stable in aqueous solutions and are active under visible light with a relatively low bias potential. PEC systems with n-type WO_3 as the photoanode and Cu or SnO_x/Sn as the cathode electrocatalyst have been demonstrated to achieve CO_2 reduction at low bias potentials.[252] A highly calorific product such as methane, which requires eight electrons, is obtained at a faradaic efficiency of 67% with a total CO_2 reduction faradaic efficiency of 71.6% on a Cu cathode. For the SnO_x/Sn cathode, a combined (CO + HCOOH) faradaic efficiency of 44.3% is obtained at +0.8 V. This verifies that judicious integration of a light-absorbing anode and a cathode co-catalyst can accomplish the reduction of CO_2 with high efficiency.

3.5.2. Monolithic cells

3.5.2.1. Photoelectrochemical diodes

Tandem absorbers have been applied in self-biasing systems.[97,184,253] The photoanode (S1) and photocathode (S2) can be integrated into a monolithic structure (so-called diode) either by stacking the two electrodes on the same substrate or by joining them together by a PCM (Figure 7e). This monolithic cell has been observed to generate H_2 by simply loading it in any water container.[254] The products are separated on both sides of the assembly. Such a strategy is successful in meter-scale panels, for which ionic transport over macroscopic distances is assumed to experience a tremendous ohmic loss. The trade-off between proton-transport distance and product separation limits the panel size. Haussener et al. have calculated the size of the standalone device and have concluded that to avoid excessive overpotentials the typical electrode size should not exceed approximately 10 mm.[255]

The photochemical diode was first reported in 1977.[253d] Later, an assembly of Si-PV junctions was built to produce hydrogen at 7.8% efficiency.[256] A similar device with earth-abundant catalysts has been examined in a neutral electrolyte with an efficiency of 2.5%.[253j] Two-photon diodes based on metal-oxide nanotubes have recently been reported.[97,253f,g,257] A n-TiO_2 nanotubes/p-Cu-Ti-O nanotubes PEC diode has been integrated with glass substrates oriented back to back. Light is incident on the UV-absorbing n-TiO_2 side and the visible light passes to the p-Cu-Ti-O side. The TiO_2 side of the diode is kept in 1 M KOH and the Cu-Ti-O side is kept in 0.1 M Na_2HPO_4 with a salt bridge linking the two sides. The reactions are powered by incident light to generate fuel with O_2 evolved from the TiO_2 side and H_2 evolved from the p-Cu-Ti-O side. A photocurrent density of 0.25 mA cm^{-2} is obtained with a photoconversion efficiency of 0.3%.[253f] The same group further proposes a ternary oxide nanotube array with a gradient composition to absorb light over different wavelengths (Figure 7f).[253g] Analysis shows that the use of a large-band-gap material in the photocathode instead of in the photoanode is desirable.[184]

To promote CO_2 reduction, a PEC diode has been designed in which the anode and cathode are separated by a PCM. The anode consists of doped TNTs for light harvesting, electron transport, and proton diffusion. The cathodic CO_2 reduction is based on Fe/N-doped carbon nanotubes deposited over a carbon cloth[253i] or Pt-modified RGO loaded on nickel foam.[253c,e] Although these devices are able to limit charge recombination, reduce the energy input, and increase the efficiency of CO_2 reduction, a bias of approximately 2.0 V is required on the basis of the redox reduction to separate the electrons and holes. The thin-film PV provides sufficient potential for the reactions, and a standalone device has shown a conversion efficiency of approximately 4.5%.[258] Unassisted two-photon devices with a wireless or wired configuration have been reported to produce solar formate with a InP/[RuCP] semiconductor/metal-complex cathode and $SrTiO_3$ anode.[253b,h,259] Electron transfer over the devices leads to STF efficiencies of 0.14 and 0.08% in the wired and wireless configurations, respectively. This indicates that the design of the band configuration is crucial for solar formate production.

3.5.2.2. All-in-one membranes

If photoactive components are extremely small NWs or NPs, they can be imbedded in a membrane as an integral part of the interface (Figure 7g).[260] Two types of such all-in-one membranes have been reported: a multifunctional membrane embedded with Si microwires and fuel-cell-like cells comprising porous electrodes.[19a,b,261] This concept offers assemblies with good light-harvesting capabilities and the possibility to tune each side individually. One or both electrodes can be exposed to the gas phase, and even flue gas or atmospheric CO_2 can be used as the input stream for the cathode side. The efficiency does not decrease if the size of cell increases.[19a] However, the membrane is easily poisoned in acidic or alkaline media. Thus, there is a strong need for research on multifunctional interfaces.

The Joint Center for Artificial Photosynthesis has developed a multifunctional membrane embedded with Si microwires. The concept modules use two different semiconductors, a wider band-gap anode material, and a narrower band-gap cathode material to yield a potential >1.23 V, which is necessary for water photolysis. Cocatalysts distributed along the semiconductor surface facilitate the reactions at low overpotentials, and two PEs are connected by a thin poly(3,4-ethylenedioxythiophene)–polystyrene sulfonate (PEDOT–PSS) layer (Figure 7h).[262] A crucial component is a Nafion proton-exchange polymer membrane.[261c,263] The membrane serves as a structural support for the silicon microwires, allows efficient proton transport while avoiding product crossover, offers an electric interconnection between the anode and cathode, and also is transparent for red wavelength photons. A second concept module, built by using experience obtained from fuel cells, imposes less stringent requirements on the interface. In such an assembly, the carbon-based gas-diffusion electrode is coated with semiconductor nanoparticles, and the counter electrode consists of metal nanoparticles deposited on a carbon substrate.[261d,e] A similar concept has been adopted to design active heterostructures that consist of a semiconductor light absorber for oxidation and alumina-coated cocatalysts for reduction. A free-floating device produces H_2 at a stable rate over 24 h with visible light as the only input and a STF efficiency of approximately 0.9%.[261a]

PEs loaded with suitable cocatalysts are important for redox reactions, and integrating the components together into a standalone device is an enormous challenge.[8c,19a,261c] A p-type Si nanopillar loaded with $[Mo_3S_4]$ clusters has been embedded in a PCM for harvesting low-energy photons in the solar spectrum. The assembly is an efficient photocathode for hydrogen generation in an aqueous 1.0 M $HClO_4$ solution, and it can achieve a photocurrent density as high as 9 mA cm^{-2} with zero overpotential.[16] This is sufficient to achieve a STF efficiency of 10% in a two-photon cell. The measured amount of hydrogen roughly matches half the number of electrons passed through the circuit, which confirms that the photocur-

rent is indeed due to photocatalytic hydrogen evolution and is not from reduction of the Mo_3S_4 clusters. Although these promising devices have been demonstrated, none of the current cells fulfill the requirements for practical application. Device modeling and thin-film deposition techniques are necessary methods to build future assemblies.[255,264]

4. Summary and Outlook

We reviewed general strategies to construct two-photon semiconducting structures toward solar-fuel applications. Particularly, we focused our discussion on essential models that dictate the performance of this technique: the indirect combination of two semiconductors by a redox couple, direct coupling of two semiconductors, multicomponent structures with a solid conductive mediator, and composite photoelectrodes together with two-photon cells. Photocatalytic and photoelectrochemical examples were selected to demonstrate these concepts from a system-level angle, and this included semiconductor particles in aqueous solution, heterogeneous photoelectrodes, and complete devices for water splitting or CO_2 conversion. Various charge-extraction schemes in solution contact systems, multicomponent structures, nanostructured photoelectrodes and photovoltaic–photoelectrochemical devices, Z-scheme cells, and monolithic cells were reviewed. Successful creation of these structures will enable us to better control local photochemical environments and will be helpful to deepen the comprehension of charge transport and utilization in the processes.

Apparent quantum yields based on various photocatalytic systems were extracted from selected articles and are shown in Figure 8a, and the solar-to-fuel conversion rates of related photoelectrochemical systems are plotted in Figure 8b. It would be more reasonable to compare the efficiencies and product yields over various systems, but such data is not readily available. The values presented are to show typical yields and are dependent upon many variables such as materials and structures, light intensity and wavelength, electrical bias, and electrolyte. In general, the rational design of functional structures that are analogous to biological systems is a promising way to improve activity. By steering charge transport, one can rationally design semiconducting structures according to specific demands. Solid-state two- or three-component semiconducting structures exhibit better performance than solution-contact structures. Optimization of the three-component structure should create great opportunity for further improvements.

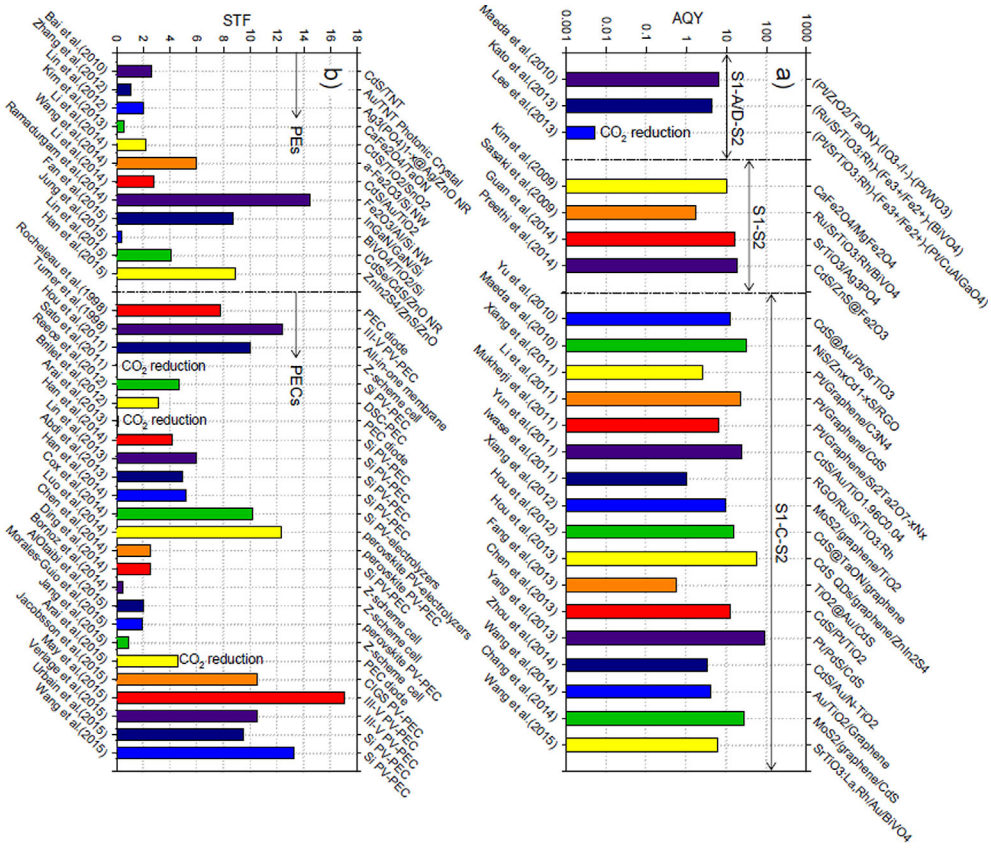

Figure 8. a) The reported apparent quantum yields on a semilogarithmic scale for photocatalytic fuel generation. b) The reported solar-to-fuel conversion efficiencies of photoelectrosynthesis. Values were taken from references given in the article. Note: Apparent quantum yields AQY% = (number of reacted electrons)/(number of incident photons) × 100% = (number of evolved hydrogen molecules × 2)/(number of incident photons) × 100%. Solar-to-fuel (STF) conversion efficiency = (output energy of hydrogen evolved)/(energy of incident solar light) × 100% = $[I_{ph}(1.23-V_{bias})\eta_F]/P_{in}$ = [(mean rate of products produced in mmol s^{-1}) × 273 kJ mol^{-1}]/[(light intensity in mW cm^{-2}) × (area in cm^2)] × 100%, in which I_{ph} is the short-circuit photocurrent density (mA cm^{-2}), η_F is the faradaic efficiency and is defined as the moles of electrons consumed in the formation of the reaction product over the total moles of electrons transferred from the anode to the cathode, and P_{in} is the incident light power intensity on the PE (mW cm^{-2}).

Reported STF efficiencies of PEC structures vary from below 1 to 18%; only a few multijunction PEC cells demonstrate a value above 10%. Compositionally integrating different materials [e.g., p-type or n-type semiconductor(s)/graphene/metals/quantum dots, etc.] with various building blocks (from nanoparticles, 1D nanowires/nanorods/nanotubes, 2D nanosheets to 3D porous or complex nanostructure) to build spatially functional structures was shown to improve light absorption and to facilitate microscopic charge transfer. Metals both in direct contact with the light absorber and in a separate but electrically connected cell serve as electron sinks and catalysts. The engineering of special interfaces to form efficient interactions such as heterojunctions and Schottky and ohmic junctions offers an effective tool to enhance charge separation and to extend charge lifetimes. Strategies to separate charges in Z-scheme catalysts and surface passivation layers require further study to understand the mechanism. The roles of plasmonic and high-energy hot electrons represent recent breakthroughs concerning our understanding of charge transfer, and more work should be paid to fully realize their potential.

Although great effort has been devoted to finding combinations of materials to steer charge transport for photosynthetic systems, much of this domain has yet to be explored. Future prospects are likely to focus on essential interface properties of the junctions and on the design of well-defined structures for optimal control of the rate, yield, and energetics of the charge carrier flow at the nanoscale so that the complete structures can achieve maximum conversion of solar energy into chemical fuels. Novel structure designs and controlled synthesis and assembly through advanced manufacturing processes such as wet-chemical synthesis with micro/nanofabrication, deposition of low-costing materials, and large-scale self-assembly will be required to meet the technology goals. This work is helpful to understand the mechanism of charge transport in semiconducting structures, and the complied information can be used to evaluate progress in the solar-fuel field and to target a research direction for future development.

Acknowledgements

The authors acknowledge financial support from the Norwegian Research Council-Independent Projects – Mathematics, Physical Science and Technology (FRINATEK) Programme (231416/F20) and the European Economic Area (EEA)-Poland (237761) Program. G.H.L. is also thankful for support from the Nature Science Foundation of China (51576002) and the Leading Talent Team in Universities of Anhui Province.

Keywords: charge transport · heterojunctions · photosynthesis · semiconductors · solar fuels

[1] a) S. Chu, A. Majumdar, *Nature* **2012**, *488*, 294 – 303; b) N. S. Lewis, D. G. Nocera, *Proc. Natl. Acad. Sci. USA* **2006**, *103*, 15729 – 15735.
[2] N. S. Lewis, *Science* **2016**, *351*, aad1920.
[3] a) W. Tu, Y. Zhou, Z. Zou, *Adv. Mater.* **2014**, *26*, 4607 – 4626; b) Y. Tachibana, L. Vayssieres, J. R. Durrant, *Nat. Photonics* **2012**, *6*, 511 – 518; c) J. L. White, M. F. Baruch, J. E. Pander, III, Y. Hu, I. C. Fortmeyer, J. E. Park, T. Zhang, K. Liao, J. Gu, Y. Yan, T. W. Shaw, E. Abelev, A. B. Bocarsly, *Chem. Rev.* **2015**, *115*, 12888 – 12935; d) Y. Ma, X. Wang, Y. Jia, X. Chen, H. Han, C. Li, *Chem. Rev.* **2014**, *114*, 9987 – 10043; e) www.rsc.org/solar-fuels, **2012**; f) X. Li, J. Yu, J. Low, Y. Fang, J. Xiao, X. Chen, *J. Mater. Chem. A* **2015**, *3*, 2485 – 2534; g) G. Liu, N. Hoivik, K. Wang, H. Jakobsen, *Sol. Energy Mater. Sol. Cells* **2012**, *105*, 53 – 68; h) A. Fujishima, K. Honda, *Nature* **1972**, *238*, 37 – 38; i) T. Inoue, A. Fujishima, S. Konishi, K. Honda, *Nature* **1979**, *277*, 637 – 638.
[4] a) J. Ran, J. Zhang, J. Yu, M. Jaroniec, S. Z. Qiao, *Chem. Soc. Rev.* **2014**, *43*, 7787 – 7812; b) S. J. A. Moniz, S. A. Shevlin, D. J. Martin, Z.-X. Guo, J. Tang, *Energy Environ. Sci.* **2015**, *8*, 731 – 759; c) A. Kudo, Y. Miseki, *Chem. Soc. Rev.* **2009**, *38*, 253 – 278; d) K. Sivula, R. van de Krol, *Nat. Rev. Mater.* **2016**, *1*, 15010.
[5] a) P. D. Tran, L. H. Wong, J. Barber, J. S. C. Loo, *Energy Environ. Sci.* **2012**, *5*, 5902; b) X. Chen, S. Shen, L. Guo, S. S. Mao, *Chem. Rev.* **2010**, *110*, 6503 – 6570; c) H. Zhou, Y. Qu, T. Zeid, X. Duan, *Energy Environ. Sci.* **2012**, *5*, 6732.
[6] a) A. V. Akimov, A. J. Neukirch, O. V. Prezhdo, *Chem. Rev.* **2013**, *113*, 4496 – 4565; b) S. C. Warren, K. Voitchovsky, H. Dotan, C. M. Leroy, M. Cornuz, F. Stellacci, C. Hebert, A. Rothschild, M. Grätzel, *Nat. Mater.* **2013**, *12*, 842 – 849; c) B. A. Pinaud, J. D. Benck, L. C. Seitz, A. J. Forman, Z. Chen, T. G. Deutsch, B. D. James, K. N. Baum, G. N. Baum, S. Ardo, H. Wang, E. Miller, T. F. Jaramillo, *Energy Environ. Sci.* **2013**, *6*, 1983.
[7] P. Liao, E. A. Carter, *Chem. Soc. Rev.* **2013**, *42*, 2401 – 2422.
[8] a) S. Dahl, I. Chorkendorff, *Nat. Mater.* **2012**, *11*, 100 – 101; b) Z. Huang, C. Xiang, H.-J. Lewerenz, N. S. Lewis, *Energy Environ. Sci.* **2014**, *7*, 1207 – 1211; c) J. R. McKone, N. S. Lewis, H. B. Gray, *Chem. Mater.* **2014**, *26*, 407 – 414.
[9] a) G. F. Moore, G. W. Brudvig, *Annu. Rev. Condens. Matter Phys.* **2011**, *2*, 303 – 327; b) H. Zhou, X. Li, T. Fan, F. E. Osterloh, J. Ding, E. M. Sabio, D. Zhang, Q. Guo, *Adv. Mater.* **2010**, *22*, 951 – 956; c) J. J. Concepcion, R. L. House, J. M. Papanikolas, T. J. Meyer, *Proc. Natl. Acad. Sci. USA* **2012**, *109*, 15560 – 15564; d) S. Bensaid, G. Centi, E. Garrone, S. Perathoner, G. Saracco, *ChemSusChem* **2012**, *5*, 500 – 521.
[10] a) K. Maeda, R. Abe, K. Domen, *J. Phys. Chem. C* **2011**, *115*, 3057 – 3064; b) D. J. Martin, P. J. Reardon, S. J. Moniz, J. Tang, *J. Am. Chem. Soc.* **2014**, *136*, 12568 – 12571.
[11] a) F. Peng, Q. Zhou, D. Zhang, C. Lu, Y. Ni, J. Kou, J. Wang, Z. Xu, *Appl. Catal. B* **2015**, *165*, 419 – 427; b) W. Yan, Y. Zhang, W. Xie, S. Sun, J. Ding, J. Bao, C. Gao, *J. Phys. Chem. C* **2014**, *118*, 6077 – 6083.
[12] a) H. Tada, T. Mitsui, T. Kiyonaga, T. Akita, K. Tanaka, *Nat. Mater.* **2006**, *5*, 782 – 786; b) A. Iwase, Y. H. Ng, Y. Ishiguro, A. Kudo, R. Amal, *J. Am. Chem. Soc.* **2011**, *133*, 11054 – 11057.
[13] Y. Hou, F. Zuo, A. Dagg, P. Feng, *Nano Lett.* **2012**, *12*, 6464 – 6473.
[14] A. Paracchino, V. Laporte, K. Sivula, M. Grätzel, E. Thimsen, *Nat. Mater.* **2011**, *10*, 456 – 461.
[15] F. F. Abdi, L. Han, A. H. Smets, M. Zeman, B. Dam, R. van de Krol, *Nat. Commun.* **2013**, *4*, 2195.
[16] Y. Hou, B. L. Abrams, P. C. Vesborg, M. E. Bjorketun, K. Herbst, L. Bech, A. M. Setti, C. D. Damsgaard, T. Pedersen, O. Hansen, J. Rossmeisl, S. Dahl, J. K. Norskov, I. Chorkendorff, *Nat. Mater.* **2011**, *10*, 434 – 438.
[17] a) R. Abe, *J. Photochem. Photobiol. C* **2010**, *11*, 179 – 209; b) K. Maeda, *ACS Catal.* **2013**, *3*, 1486 – 1503.
[18] a) P. Zhou, J. Yu, M. Jaroniec, *Adv. Mater.* **2014**, *26*, 4920 – 4935; b) H. Li, Y. Zhou, W. Tu, J. Ye, Z. Zou, *Adv. Funct. Mater.* **2015**, *25*, 998 – 1013.
[19] a) J. Rongé, T. Bosserez, D. Martel, C. Nervi, L. Boarino, F. Taulelle, G. Decher, S. Bordiga, J. A. Martens, *Chem. Soc. Rev.* **2014**, *43*, 7963 – 7981; b) K. S. Joya, Y. F. Joya, K. Ocakoglu, R. van de Krol, *Angew. Chem. Int. Ed.* **2013**, *52*, 10426 – 10437; *Angew. Chem.* **2013**, *125*, 10618 – 10630; c) Z. Xing, X. Zong, J. Pan, L. Wang, *Chem. Eng. Sci.* **2013**, *104*, 125 – 146.
[20] H. Park, H.-i. Kim, G.-h. Moon, W. Choi, *Energy Environ. Sci.* **2016**, *9*, 411 – 433.
[21] a) K. Kalyanasundaram, M. Graetzel, *Curr. Opin. Biotechnol.* **2010**, *21*, 298 – 310; b) J. Barber, P. D. Tran, *J. R. Soc. Interface* **2013**, *10*, 20120984; c) J. Barber, *Chem. Soc. Rev.* **2009**, *38*, 185 – 196.
[22] A. D. Handoko, K. Li, J. Tang, *Curr. Opin. Chem. Eng.* **2013**, *2*, 200 – 206.
[23] R. Marschall, *Adv. Funct. Mater.* **2014**, *24*, 2421 – 2440.
[24] Y.-P. Yuan, L.-W. Ruan, J. Barber, S. C. Joachim Loo, C. Xue, *Energy Environ. Sci.* **2014**, *7*, 3934 – 3951.
[25] A. Kudo, *MRS Bull.* **2011**, *36*, 32 – 38.

[26] A. J. Bard, *J. Photochem.* **1979**, *10*, 59 – 75.
[27] a) R. Abe, M. Higashi, K. Domen, *ChemSusChem* **2011**, *4*, 228 – 237; b) K. Maeda, M. Higashi, D. L. Lu, R. Abe, K. Domen, *J. Am. Chem. Soc.* **2010**, *132*, 5858 – 5868.
[28] M. Tabata, K. Maeda, M. Higashi, D. Lu, T. Takata, R. Abe, K. Domen, *Langmuir* **2010**, *26*, 9161 – 9165.
[29] a) K. Maeda, D. Lu, K. Domen, *ACS Catal.* **2013**, *3*, 1026 – 1033; b) M. Higashi, R. Abe, T. Takata, K. Domen, *Chem. Mater.* **2009**, *21*, 1543 – 1549.
[30] S. Hara, M. Yoshimizu, S. Tanigawa, L. Ni, B. Ohtani, H. Irie, *J. Phys. Chem. C* **2012**, *116*, 17458 – 17463.
[31] a) R. Abe, K. Shinmei, N. Koumura, K. Hara, B. Ohtani, *J. Am. Chem. Soc.* **2013**, *135*, 16872 – 16884; b) R. Abe, K. Shinmei, K. Hara, B. Ohtani, *Chem. Commun.* **2009**, 3577 – 3579.
[32] a) J. Yang, D. Wang, H. Han, C. Li, *Acc. Chem. Res.* **2013**, *46*, 1900 – 1909; b) Y. Sasaki, A. Iwase, H. Kato, A. Kudo, *J. Catal.* **2008**, *259*, 133 – 137.
[33] H. Kato, Y. Sasaki, N. Shirakura, A. Kudo, *J. Mater. Chem. A* **2013**, *1*, 12327.
[34] Y. Sasaki, H. Kato, A. Kudo, *J. Am. Chem. Soc.* **2013**, *135*, 5441 – 5449.
[35] B. Fujihara, T. Ohno, M. Matsumura, *J. Chem. Soc. Faraday Trans.* **1998**, *94*, 3705 – 3709.
[36] S. W. Bae, S. M. Ji, S. J. Hong, J. W. Jang, J. S. Lee, *Int. J. Hydrogen Energy* **2009**, *34*, 3243 – 3249.
[37] a) C.-C. Lo, C.-W. Huang, C.-H. Liao, J. C. S. Wu, *Int. J. Hydrogen Energy* **2010**, *35*, 1523 – 1529; b) W.-H. Lee, C.-H. Liao, M.-F. Tsai, C.-W. Huang, J. C. S. Wu, *Appl. Catal. B* **2013**, *132 – 133*, 445 – 451; c) S.-C. Yu, C.-W. Huang, C.-H. Liao, J. C. S. Wu, S.-T. Chang, K.-H. Chen, *J. Membr. Sci.* **2011**, *382*, 291 – 299.
[38] a) W. Fan, Q. Zhang, Y. Wang, *Phys. Chem. Chem. Phys.* **2013**, *15*, 2632 – 2649; b) S. Bai, J. Jiang, Q. Zhang, Y. Xiong, *Chem. Soc. Rev.* **2015**, *44*, 2893 – 2939.
[39] X. Yao, T. Liu, X. Liu, L. Lu, *Chem. Eng. J.* **2014**, *255*, 28 – 39.
[40] a) H. N. Kim, T. W. Kim, I. Y. Kim, S.-J. Hwang, *Adv. Funct. Mater.* **2011**, *21*, 3111 – 3118; b) D. W. Jing, L. J. Guo, *J. Phys. Chem. C* **2007**, *111*, 13437 – 13441.
[41] a) J. Ryu, S. H. Lee, D. H. Nam, C. B. Park, *Adv. Mater.* **2011**, *23*, 1883 – 1888; b) L. Long, X. Yu, L. Wu, J. Li, X. Li, *Nanotechnology* **2014**, *25*, 035603; c) C. Li, J. Yuan, B. Han, L. Jiang, W. Shangguan, *Int. J. Hydrogen Energy* **2010**, *35*, 7073 – 7079.
[42] Z. Zheng, W. Xie, Z. S. Lim, L. You, J. Wang, *Sci. Rep.* **2014**, *4*, 5721.
[43] X. Guan, L. Guo, *ACS Catal.* **2014**, *4*, 3020 – 3026.
[44] J. Lv, T. Kako, Z. S. Li, Z. G. Zou, J. H. Ye, *J. Phys. Chem. C* **2010**, *114*, 6157 – 6162.
[45] a) Z. Wang, A. Shakya, J. Gu, S. Lian, S. Maldonado, *J. Am. Chem. Soc.* **2013**, *135*, 9275 – 9278; b) K. Zheng, K. Žídek, M. Abdellah, W. Zhang, P. Chábera, N. Lenngren, A. Yartsev, T. Pullerits, *J. Phys. Chem. C* **2014**, *118*, 18462 – 18471.
[46] X. Li, H. Liu, D. Luo, J. Li, Y. Huang, H. Li, Y. Fang, Y. Xu, L. Zhu, *Chem. Eng. J.* **2012**, *180*, 151 – 158.
[47] C. Wang, R. L. Thompson, P. Ohodnicki, J. Baltrus, C. Matranga, *J. Mater. Chem.* **2011**, *21*, 13452.
[48] M. Abou Asi, C. He, M. Su, D. Xia, L. Lin, H. Deng, Y. Xiong, R. Qiu, X.-z. Li, *Catal. Today* **2011**, *175*, 256 – 263.
[49] M. F. Ehsan, T. He, *Appl. Catal. B* **2015**, *166 – 167*, 345 – 352.
[50] M. F. Ehsan, M. N. Ashiq, F. Bi, Y. Bi, S. Palanisamy, T. He, *RSC Adv.* **2014**, *4*, 48411 – 48418.
[51] K. Tvrdy, P. A. Frantsuzov, P. V. Kamat, *Proc. Natl. Acad. Sci. USA* **2011**, *108*, 29 – 34.
[52] a) E. Najafi, T. D. Scarborough, J. Tang, A. Zewail, *Science* **2015**, *347*, 164 – 167; b) S. Ida, A. Takashiba, S. Koga, H. Hagiwara, T. Ishihara, *J. Am. Chem. Soc.* **2014**, *136*, 1872 – 1878.
[53] A. Kezzim, N. Nasrallah, A. Abdi, M. Trari, *Energy Convers. Manage.* **2011**, *52*, 2800 – 2806.
[54] H. Xu, S. Ouyang, L. Liu, D. Wang, T. Kako, J. Ye, *Nanotechnology* **2014**, *25*, 165402.
[55] A. Kubacka, M. J. Muñoz-Batista, M. Fernández-García, S. Obregón, G. Colón, *Appl. Catal. B* **2015**, *163*, 214 – 222.
[56] S. I. In, D. D. Vaughn, 2nd, R. E. Schaak, *Angew. Chem. Int. Ed.* **2012**, *51*, 3915 – 3918; *Angew. Chem.* **2012**, *124*, 3981 – 3984.
[57] J. Zhang, S. Z. Qiao, L. Qi, J. Yu, *Phys. Chem. Chem. Phys.* **2013**, *15*, 12088 – 12094.
[58] A. Nashim, K. Parida, *J. Mater. Chem. A* **2014**, *2*, 18405 – 18412.
[59] H. G. Kim, P. H. Borse, W. Choi, J. S. Lee, *Angew. Chem. Int. Ed.* **2005**, *44*, 4585 – 4589; *Angew. Chem.* **2005**, *117*, 4661 – 4665.
[60] H. G. Kim, P. H. Borse, J. S. Jang, E. D. Jeong, O. S. Jung, Y. J. Suh, J. S. Lee, *Chem. Commun.* **2009**, 5889 – 5891.
[61] J. Zhang, M. Zhang, R. Q. Sun, X. Wang, *Angew. Chem. Int. Ed.* **2012**, *51*, 10145 – 10149; *Angew. Chem.* **2012**, *124*, 10292 – 10296.
[62] Y. Wang, B. Li, C. Zhang, L. Cui, S. Kang, X. Li, L. Zhou, *Appl. Catal. B* **2013**, *130 – 131*, 277 – 284.
[63] G. Xi, S. Ouyang, J. Ye, *Chem. Eur. J.* **2011**, *17*, 9057 – 9061.
[64] L. Xu, J. Guan, L. Gao, Z. Sun, *Catal. Commun.* **2011**, *12*, 548 – 552.
[65] J. Chen, S. Shen, P. Guo, M. Wang, P. Wu, X. Wang, L. Guo, *Appl. Catal. B* **2014**, *152 – 153*, 335 – 341.
[66] S.-W. Cao, X.-F. Liu, Y.-P. Yuan, Z.-Y. Zhang, Y.-S. Liao, J. Fang, S. C. J. Loo, T. C. Sum, C. Xue, *Appl. Catal. B* **2014**, *147*, 940 – 946.
[67] S. Zhou, Y. Liu, J. Li, Y. Wang, G. Jiang, Z. Zhao, D. Wang, A. Duan, J. Liu, Y. Wei, *Appl. Catal. B* **2014**, *158 – 159*, 20 – 29.
[68] Y. He, Y. Wang, L. Zhang, B. Teng, M. Fan, *Appl. Catal. B* **2015**, *168 – 169*, 1 – 8.
[69] a) L. Xu, E. M. P. Steinmiller, S. E. Skrabalak, *J. Phys. Chem. C* **2012**, *116*, 871 – 877; b) N. Siedl, S. O. Baumann, M. J. Elser, O. Diwald, *J. Phys. Chem. C* **2012**, *116*, 22967 – 22973.
[70] J. Yan, G. Wu, N. Guan, L. Li, *Appl. Catal. B* **2014**, *152 – 153*, 280 – 288.
[71] P. Dhanasekaran, H. G. Salunke, N. M. Gupta, *J. Phys. Chem. C* **2012**, *116*, 12156 – 12164.
[72] Q. Tian, W. Wu, L. Sun, S. Yang, M. Lei, J. Zhou, Y. Liu, X. Xiao, F. Ren, C. Jiang, V. A. Roy, *ACS Appl. Mater. Interfaces* **2014**, *6*, 13088 – 13097.
[73] J. Sun, X. Li, Q. Zhao, J. Ke, D. Zhang, *J. Phys. Chem. C* **2014**, *118*, 10113 – 10121.
[74] V. Preethi, S. Kanmani, *Int. J. Hydrogen Energy* **2014**, *39*, 1613 – 1622.
[75] E. A. Kozlova, D. V. Markovskaya, S. V. Cherepanova, A. A. Saraev, E. Y. Gerasimov, T. V. Perevalov, V. V. Kaichev, V. N. Parmon, *Int. J. Hydrogen Energy* **2014**, *39*, 18758 – 18769.
[76] X. Wang, J. Chen, X. Guan, L. Guo, *Int. J. Hydrogen Energy* **2015**, *40*, 7546 – 7552.
[77] J.-P. Zou, S.-L. Lei, J. Yu, S.-L. Luo, X.-B. Luo, X.-H. Tang, W.-L. Dai, J. Sun, G.-C. Guo, C.-T. Au, *Appl. Catal. B* **2014**, *150 – 151*, 466 – 471.
[78] T. P. Lyubina, D. V. Markovskaya, E. A. Kozlova, V. N. Parmon, *Int. J. Hydrogen Energy* **2013**, *38*, 14172 – 14179.
[79] Z.-J. Jiang, D. F. Kelley, *J. Phys. Chem. C* **2012**, *116*, 12958 – 12968.
[80] D. Perera, R. Lorek, R. S. Khnayzer, P. Moroz, T. O'Connor, D. Khon, G. Diederich, E. Kinder, S. Lambright, F. N. Castellano, M. Zamkov, *J. Phys. Chem. C* **2012**, *116*, 22786 – 22793.
[81] S. Balachandran, N. Prakash, K. Thirumalai, M. Muruganandham, M. Sillanpää, M. Swaminathan, *Ind. Eng. Chem. Res.* **2014**, *53*, 8346 – 8356.
[82] J. Su, X.-X. Zou, G.-D. Li, X. Wei, C. Yan, Y.-N. Wang, J. Zhao, L.-J. Zhou, J.-S. Chen, *J. Phys. Chem. C* **2011**, *115*, 8064 – 8071.
[83] X. Li, J. Chen, H. Li, J. Li, Y. Xu, Y. Liu, J. Zhou, *J. Nat. Gas Chem.* **2011**, *20*, 413 – 417.
[84] a) H. Bai, Z. Liu, D. D. Sun, H. Du, *J. Am. Ceram. Soc.* **2013**, *96*, 942 – 949; b) J. Ng, S. Xu, X. Zhang, H. Y. Yang, D. D. Sun, *Adv. Funct. Mater.* **2010**, *20*, 4287 – 4294.
[85] a) L. Huang, X. Wang, J. Yang, G. Liu, J. Han, C. Li, *J. Phys. Chem. C* **2013**, *117*, 11584 – 11591; b) P. Tongying, V. V. Plashnitsa, N. Petchsang, F. Vietmeyer, G. J. Ferraudi, G. Krylova, M. Kuno, *J. Phys. Chem. Lett.* **2012**, *3*, 3234 – 3240; c) J. Huang, K. L. Mulfort, P. Du, L. X. Chen, *J. Am. Chem. Soc.* **2012**, *134*, 16472 – 16475.
[86] A. Thibert, F. A. Frame, E. Busby, M. A. Holmes, F. E. Osterloh, D. S. Larsen, *J. Phys. Chem. Lett.* **2011**, *2*, 2688 – 2694.
[87] Z. Pan, H. Zhang, K. Cheng, Y. Hou, J. Hua, X. Zhong, *ACS Nano* **2012**, *6*, 3982 – 3991.
[88] X. Yang, J. Xu, T. Wong, Q. Yang, C. S. Lee, *Phys. Chem. Chem. Phys.* **2013**, *15*, 12688 – 12693.
[89] E. Khon, K. Lambright, R. S. Khnayzer, P. Moroz, D. Perera, E. Butaeva, S. Lambright, F. N. Castellano, M. Zamkov, *Nano Lett.* **2013**, *13*, 2016 – 2023.
[90] K. Wu, Q. Li, Y. Jia, J. R. McBride, Z. X. Xie, T. Lian, *ACS Nano* **2015**, *9*, 961 – 968.
[91] a) G. Song, F. Xin, X. Yin, *J. Colloid Interface Sci.* **2015**, *442*, 60 – 66; b) F. Xu, W. Xiao, B. Cheng, J. Yu, *Int. J. Hydrogen Energy* **2014**, *39*, 15394 –

15402; c) X. Wang, G. Liu, Z. G. Chen, F. Li, L. Wang, G. Q. Lu, H. M. Cheng, *Chem. Commun.* **2009**, 3452 – 3454.
[92] X. Wang, G. Liu, G. Q. Lu, H.-M. Cheng, *Int. J. Hydrogen Energy* **2010**, *35*, 8199 – 8205.
[93] a) Y. Sasaki, H. Nemoto, K. Saito, A. Kudo, *J. Phys. Chem. C* **2009**, *113*, 17536 – 17542; b) Q. Jia, A. Iwase, A. Kudo, *Chem. Sci.* **2014**, *5*, 1513.
[94] L. J. Zhang, S. Li, B. K. Liu, D. J. Wang, T. F. Xie, *ACS Catal.* **2014**, *4*, 3724 – 3729.
[95] H. Katsumata, Y. Tachi, T. Suzuki, S. Kaneco, *RSC Adv.* **2014**, *4*, 21405.
[96] Y. Peng, Z. Guo, J. Yang, D. Wang, W. Yuan, *J. Mater. Chem. A* **2014**, *2*, 6296.
[97] C. Liu, J. Tang, H. M. Chen, B. Liu, P. Yang, *Nano Lett.* **2013**, *13*, 2989 – 2992.
[98] D. O. Scanlon, C. W. Dunnill, J. Buckeridge, S. A. Shevlin, A. J. Logsdail, S. M. Woodley, C. R. Catlow, M. J. Powell, R. G. Palgrave, I. P. Parkin, G. W. Watson, T. W. Keal, P. Sherwood, A. Walsh, A. A. Sokol, *Nat. Mater.* **2013**, *12*, 798 – 801.
[99] a) G. Marcì, E. I. García-López, L. Palmisano, *Catal. Commun.* **2014**, *53*, 38 – 41; b) S. Qin, F. Xin, Y. Liu, X. Yin, W. Ma, *J. Colloid Interface Sci.* **2011**, *356*, 257 – 261; c) Y. He, L. Zhang, M. Fan, X. Wang, M. L. Walbridge, Q. Nong, Y. Wu, L. Zhao, *Sol. Energy Mater. Sol. Cells* **2015**, *137*, 175 – 184.
[100] a) Y. Liu, G. Ji, M. A. Dastageer, L. Zhu, J. Wang, B. Zhang, X. Chang, M. A. Gondal, *RSC Adv.* **2014**, *4*, 56961 – 56969; b) C. Liu, N. P. Dasgupta, P. Yang, *Chem. Mater.* **2014**, *26*, 415 – 422.
[101] a) H. Li, Y. Gao, Y. Zhou, F. Fan, Q. Han, Q. Xu, X. Wang, M. Xiao, C. Li, Z. Zou, *Nano Lett.* **2016**, DOI: 10.1021/acs.nanolett.6b02094; b) H. Zhou, T. X. Fan, D. Zhang, *ChemCatChem* **2011**, *3*, 513 – 528.
[102] J. C. White, P. K. Dutta, *J. Phys. Chem. C* **2011**, *115*, 2938 – 2947.
[103] a) S. Linic, P. Christopher, D. B. Ingram, *Nat. Mater.* **2011**, *10*, 911 – 921; b) C. Clavero, *Nat. Photonics* **2014**, *8*, 95 – 103.
[104] a) K. Wu, Z. Chen, H. Lv, H. Zhu, C. L. Hill, T. Lian, *J. Am. Chem. Soc.* **2014**, *136*, 7708 – 7716; b) J. S. Jang, S. H. Choi, H. G. Kim, J. S. Lee, *J. Phys. Chem. C* **2008**, *112*, 17200 – 17205.
[105] a) H. Park, W. Choi, M. R. Hoffmann, *J. Mater. Chem.* **2008**, *18*, 2379; b) J. Chen, H. Su, Y. Liu, Y. Zeng, W. Zhang, J. Gu, W. M. Lau, D. Zhang, *Int. J. Hydrogen Energy* **2013**, *38*, 8639 – 8647.
[106] K. Li, B. Chai, T. Peng, J. Mao, L. Zan, *ACS Catal.* **2013**, *3*, 170 – 177.
[107] Y. Zhu, Z. Chen, T. Gao, Q. Huang, F. Niu, L. Qin, P. Tang, Y. Huang, Z. Sha, Y. Wang, *Appl. Catal. B* **2015**, *163*, 16 – 22.
[108] J. Yang, H. Yan, X. Wang, F. Wen, Z. Wang, D. Fan, J. Shi, C. Li, *J. Catal.* **2012**, *290*, 151 – 157.
[109] J. Fang, L. Xu, Z. Zhang, Y. Yuan, S. Cao, Z. Wang, L. Yin, Y. Liao, C. Xue, *ACS Appl. Mater. Interfaces* **2013**, *5*, 8088 – 8092.
[110] Y.-C. Chen, Y.-C. Pu, Y.-J. Hsu, *J. Phys. Chem. C* **2012**, *116*, 2967 – 2975.
[111] R. Zhang, J. Wang, P. Han, *J. Alloys Compd.* **2015**, *637*, 483 – 488.
[112] D. Wang, T. Hisatomi, T. Takata, C. Pan, M. Katayama, J. Kubota, K. Domen, *Angew. Chem. Int. Ed.* **2013**, *52*, 11252 – 11256; *Angew. Chem.* **2013**, *125*, 11462 – 11466.
[113] a) T. O'Connor, M. S. Panov, A. Mereshchenko, A. N. Tarnovsky, R. Lorek, D. Perera, G. Diederich, S. Lambright, P. Moroz, M. Zamkov, *ACS Nano* **2012**, *6*, 8156 – 8165; b) K. P. Acharya, R. S. Khnayzer, T. O'Connor, G. Diederich, M. Kirsanova, A. Klinkova, D. Roth, E. Kinder, M. Imboden, M. Zamkov, *Nano Lett.* **2011**, *11*, 2919 – 2926.
[114] S. Xie, Y. Wang, Q. Zhang, W. Fan, W. Deng, Y. Wang, *Chem. Commun.* **2013**, *49*, 2451 – 2453.
[115] Q. Kang, T. Wang, P. Li, L. Liu, K. Chang, M. Li, J. Ye, *Angew. Chem. Int. Ed.* **2015**, *54*, 841 – 845; *Angew. Chem.* **2015**, *127*, 855 – 859.
[116] a) Q. Wang, X. Yang, D. Liu, L. Chi, J. Hou, *Electrochim. Acta* **2012**, *83*, 140 – 145; b) K. Xie, Q. Wu, Y. Wang, W. Guo, M. Wang, L. Sun, C. Lin, *Electrochem. Commun.* **2011**, *13*, 1469 – 1472.
[117] Q. C. Xu, Y. H. Ng, Y. Zhang, J. S. Loo, R. Amal, T. T. Tan, *Chem. Commun.* **2011**, *47*, 8641 – 8643.
[118] Q. Wang, T. Hisatomi, S. S. K. Ma, Y. Li, K. Domen, *Chem. Mater.* **2014**, *26*, 4144 – 4150.
[119] Q. Wang, Y. Li, T. Hisatomi, M. Nakabayashi, N. Shibata, J. Kubota, K. Domen, *J. Catal.* **2015**, *328*, 308 – 315.
[120] Q. Wang, T. Hisatomi, Q. Jia, H. Tokudome, M. Zhong, C. Wang, Z. Pan, T. Takata, M. Nakabayashi, N. Shibata, Y. Li, I. D. Sharp, A. Kudo, T. Yamada, K. Domen, *Nat. Mater.* **2016**, *15*, 611 – 615.
[121] Y. Yamada, C. K. Tsung, W. Huang, Z. Huo, S. E. Habas, T. Soejima, C. E. Aliaga, G. A. Somorjai, P. Yang, *Nat. Chem.* **2011**, *3*, 372 – 376.
[122] S. Sun, X. Chang, L. Dong, Y. Zhang, Z. Li, Y. Qiu, *J. Solid State Chem.* **2011**, *184*, 2190 – 2195.
[123] X. Hu, X. Zhou, R. Wang, C. Hu, J. Qu, *Appl. Catal. B* **2014**, *154 – 155*, 44 – 50.
[124] a) M. R. Elahifard, S. Rahimnejad, S. Haghighi, M. R. Gholami, *J. Am. Chem. Soc.* **2007**, *129*, 9552 – 9553; b) Y. Zhang, Z.-R. Tang, X. Fu, Y.-J. Xu, *Appl. Catal. B* **2011**, *106*, 445 – 452.
[125] a) Y. Hou, X. Li, Q. Zhao, G. Chen, C. L. Raston, *Environ. Sci. Technol.* **2012**, *46*, 4042 – 4050; b) Y. Hou, X. Li, Q. Zhao, X. Quan, G. Chen, *J. Mater. Chem.* **2011**, *21*, 18067.
[126] L. Zhang, K.-H. Wong, Z. Chen, J. C. Yu, J. Zhao, C. Hu, C.-Y. Chan, P.-K. Wong, *Appl. Catal. A* **2009**, *363*, 221 – 229.
[127] Y. Yang, W. Guo, Y. Guo, Y. Zhao, X. Yuan, Y. Guo, *J. Hazard. Mater.* **2014**, *271*, 150 – 159.
[128] G. Tian, Y. Chen, X. Meng, J. Zhou, W. Zhou, K. Pan, C. Tian, Z. Ren, H. Fu, *ChemPlusChem* **2013**, *78*, 117 – 123.
[129] Z. Chen, W. Wang, Z. Zhang, X. Fang, *J. Phys. Chem. C* **2013**, *117*, 19346 – 19352.
[130] Y. Bu, Z. Chen, C. Sun, *Appl. Catal. B* **2015**, *179*, 363 – 371.
[131] H. Lin, J. Cao, B. Luo, B. Xu, S. Chen, *Catal. Commun.* **2012**, *21*, 91 – 95.
[132] J. Song, Y. Shi, M. Ren, G. Hu, *Appl. Phys. A* **2014**, *116*, 2139 – 2147.
[133] R. Kobayashi, S. Tanigawa, T. Takashima, B. Ohtani, H. Irie, *J. Phys. Chem. C* **2014**, *118*, 22450 – 22456.
[134] Y. He, L. Zhang, B. Teng, M. Fan, *Environ. Sci. Technol.* **2015**, *49*, 649 – 656.
[135] H. G. Kim, E. D. Jeong, P. H. Borse, S. Jeon, K. Yong, J. S. Lee, W. Li, S. H. Oh, *Appl. Phys. Lett.* **2006**, *89*, 064103.
[136] a) L. Ding, H. Zhou, S. Lou, J. Ding, D. Zhang, H. Zhu, T. Fan, *Int. J. Hydrogen Energy* **2013**, *38*, 8244 – 8253; b) H. Zhao, M. Wu, J. Liu, Z. Deng, Y. Li, B.-L. Su, *Appl. Catal. B* **2016**, *184*, 182 – 190.
[137] H. Zhou, L. Ding, T. Fan, J. Ding, D. Zhang, Q. Guo, *Appl. Catal. B* **2014**, *147*, 221 – 228.
[138] H. Zhou, J. Pan, L. Ding, Y. Tang, J. Ding, Q. Guo, T. Fan, D. Zhang, *Int. J. Hydrogen Energy* **2014**, *39*, 16293 – 16301.
[139] M. Kim, Y. K. Kim, S. K. Lim, S. Kim, S.-I. In, *Appl. Catal. B* **2015**, *166 – 167*, 423 – 431.
[140] a) H. J. Yun, H. Lee, N. D. Kim, D. M. Lee, S. Yu, J. Yi, *ACS Nano* **2011**, *5*, 4084 – 4090; b) S. Yu, S. Y. Lee, J. Yeo, J. W. Han, J. Yi, *J. Phys. Chem. C* **2014**, *118*, 29583 – 29590.
[141] Z. B. Yu, Y. P. Xie, G. Liu, G. Q. Lu, X. L. Ma, H.-M. Cheng, *J. Mater. Chem. A* **2013**, *1*, 2773.
[142] X. Wang, G. Liu, L. Wang, Z.-G. Chen, G. Q. M. Lu, H.-M. Cheng, *Adv. Energy Mater.* **2012**, *2*, 42 – 46.
[143] Q. Zhai, S. Xie, W. Fan, Q. Zhang, Y. Wang, W. Deng, Y. Wang, *Angew. Chem. Int. Ed.* **2013**, *52*, 5776 – 5779; *Angew. Chem.* **2013**, *125*, 5888 – 5891.
[144] Y. C. Wei, J. Q. Jiao, Z. Zhao, W. J. Zhong, J. M. Li, J. Liu, G. Y. Jiang, A. J. Duan, *J. Mater. Chem. A* **2015**, *3*, 11074 – 11085.
[145] a) K. Maeda, K. Teramura, D. Lu, N. Saito, Y. Inoue, K. Domen, *Angew. Chem. Int. Ed.* **2006**, *45*, 7806 – 7809; *Angew. Chem.* **2006**, *118*, 7970 – 7973; b) T. Ikeda, A. Xiong, T. Yoshinaga, K. Maeda, K. Domen, T. Teranishi, *J. Phys. Chem. C* **2013**, *117*, 2467 – 2473; c) M. Yoshida, K. Takanabe, K. Maeda, A. Ishikawa, J. Kubota, Y. Sakata, Y. Ikezawa, K. Domen, *J. Phys. Chem. C* **2009**, *113*, 10151 – 10157.
[146] W. Li, C. Feng, S. Dai, J. Yue, F. Hua, H. Hou, *Appl. Catal. B* **2015**, *168 – 169*, 465 – 471.
[147] O. K. Varghese, M. Paulose, T. J. Latempa, C. A. Grimes, *Nano Lett.* **2009**, *9*, 731 – 737.
[148] a) B. Y. Zheng, H. Zhao, A. Manjavacas, M. McClain, P. Nordlander, N. J. Halas, *Nat. Commun.* **2015**, *6*, 7797; b) R. Long, K. Mao, M. Gong, S. Zhou, J. Hu, M. Zhi, Y. You, S. Bai, J. Jiang, Q. Zhang, X. Wu, Y. Xiong, *Angew. Chem. Int. Ed.* **2014**, *53*, 3205 – 3209; *Angew. Chem.* **2014**, *126*, 3269 – 3273; c) L. Weng, H. Zhang, A. O. Govorov, M. Ouyang, *Nat. Commun.* **2014**, *5*, 4792.
[149] a) J. Zhang, C. Niu, J. Ke, L. Zhou, G. Zeng, *Catal. Commun.* **2015**, *59*, 30 – 34; b) Z. Li, J. Liu, D. Wang, Y. Gao, J. Shen, *Int. J. Hydrogen Energy* **2012**, *37*, 6431 – 6437; c) X. Wang, S. Li, Y. Ma, H. Yu, J. Yu, *J. Phys. Chem. C* **2011**, *115*, 14648 – 14655; d) J. Hou, Z. Wang, C. Yang, W. Zhou, S. Jiao, H. Zhu, *J. Phys. Chem. C* **2013**, *117*, 5132 – 5141; e) S. Yu,

Y. H. Kim, S. Y. Lee, H. D. Song, J. Yi, *Angew. Chem. Int. Ed.* **2014**, *53*, 11203 – 11207; *Angew. Chem.* **2014**, *126*, 11385 – 11389; f) B. D. Mankidy, B. Joseph, V. K. Gupta, *Nanotechnology* **2013**, *24*, 405402; g) H. Cheng, J. Hou, H. Zhu, X.-M. Guo, *RSC Adv.* **2014**, *4*, 41622 – 41630; h) J. Hou, C. Yang, Z. Wang, Q. Ji, Y. Li, G. Huang, S. Jiao, H. Zhu, *Appl. Catal. B* **2013**, *142 – 143*, 579 – 589; i) L. Ye, J. Liu, C. Gong, L. Tian, T. Peng, L. Zan, *ACS Catal.* **2012**, *2*, 1677 – 1683; j) W.-J. Ong, L. K. Putri, L.-L. Tan, S.-P. Chai, S.-T. Yong, *Appl. Catal. B* **2016**, *180*, 530 – 543.

[150] a) A. K. Geim, *Science* **2009**, *324*, 1530 – 1534; b) K. S. Novoselov, V. I. Fal'ko, L. Colombo, P. R. Gellert, M. G. Schwab, K. Kim, *Nature* **2012**, *490*, 192 – 200.

[151] a) G. Xie, K. Zhang, B. Guo, Q. Liu, L. Fang, J. R. Gong, *Adv. Mater.* **2013**, *25*, 3820 – 3839; b) W. Tu, Y. Zhou, Z. Zou, *Adv. Funct. Mater.* **2013**, *23*, 4996 – 5008.

[152] I. V. Lightcap, T. H. Kosel, P. V. Kamat, *Nano Lett.* **2010**, *10*, 577 – 583.

[153] a) H. Li, X. Cui, *Int. J. Hydrogen Energy* **2014**, *39*, 19877 – 19886; b) L. Zhang, Z. Xi, M. Xing, J. Zhang, *Int. J. Hydrogen Energy* **2013**, *38*, 9169 – 9177.

[154] Q. Xiang, J. Yu, M. Jaroniec, *J. Phys. Chem. C* **2011**, *115*, 7355 – 7363.

[155] Q. Li, B. Guo, J. Yu, J. Ran, B. Zhang, H. Yan, J. R. Gong, *J. Am. Chem. Soc.* **2011**, *133*, 10878 – 10884.

[156] A. Mukherji, B. Seger, G. Q. Lu, L. Z. Wang, *ACS Nano* **2011**, *5*, 3483 – 3492.

[157] P. Gao, Z. Liu, D. D. Sun, *J. Mater. Chem. A* **2013**, *1*, 14262.

[158] X.-J. Lv, S.-X. Zhou, C. Zhang, H.-X. Chang, Y. Chen, W.-F. Fu, *J. Mater. Chem.* **2012**, *22*, 18542.

[159] L.-L. Tan, W.-J. Ong, S.-P. Chai, A. R. Mohamed, *Appl. Catal. B* **2015**, *166 – 167*, 251 – 259.

[160] J. Hou, H. Cheng, O. Takeda, H. Zhu, *Angew. Chem. Int. Ed.* **2015**, *54*, 8480 – 8484; *Angew. Chem.* **2015**, *127*, 8600 – 8604.

[161] Y. Hou, F. Zuo, Q. Ma, C. Wang, L. Bartels, P. Feng, *J. Phys. Chem. C* **2012**, *116*, 20132 – 20139.

[162] Y. Min, G. He, Q. Xu, Y. Chen, *J. Mater. Chem. A* **2014**, *2*, 1294 – 1301.

[163] Y. Wang, J. Yu, W. Xiao, Q. Li, *J. Mater. Chem. A* **2014**, *2*, 3847.

[164] Y. Yang, E. Liu, H. Dai, L. Kang, H. Wu, J. Fan, X. Hu, H. Liu, *Int. J. Hydrogen Energy* **2014**, *39*, 7664 – 7671.

[165] F. Meng, S. K. Cushing, J. Li, S. Hao, N. Wu, *ACS Catal.* **2015**, *5*, 1949 – 1955.

[166] S. Song, B. Cheng, N. Wu, A. Meng, S. Cao, J. Yu, *Appl. Catal. B* **2016**, *181*, 71 – 78.

[167] H. Zhang, X. Fan, X. Quan, S. Chen, H. Yu, *Environ. Sci. Technol.* **2011**, *45*, 5731 – 5736.

[168] Y. Yan, C. Wang, X. Yan, L. Xiao, J. He, W. Gu, W. Shi, *J. Phys. Chem. C* **2014**, *118*, 23519 – 23526.

[169] T. M. Suzuki, A. Iwase, H. Tanaka, S. Sato, A. Kudo, T. Morikawa, *J. Mater. Chem. A* **2015**, *3*, 13283 – 13290.

[170] K. Iwashina, A. Iwase, Y. H. Ng, R. Amal, A. Kudo, *J. Am. Chem. Soc.* **2015**, *137*, 604 – 607.

[171] a) X. Wang, X. Yao, *Carbon* **2014**, *77*, 667 – 674; b) X. Wang, L. Yin, G. Liu, *Chem. Commun.* **2014**, *50*, 3460 – 3463.

[172] P. Li, Y. Zhou, H. Li, Q. Xu, X. Meng, X. Wang, M. Xiao, Z. Zou, *Chem. Commun.* **2015**, *51*, 800 – 803.

[173] a) Q. Xiang, J. Yu, M. Jaroniec, *J. Am. Chem. Soc.* **2012**, *134*, 6575 – 6578; b) Y. Li, H. Wang, S. Peng, *J. Phys. Chem. C* **2014**, *118*, 19842 – 19848; c) K. Chang, Z. Mei, T. Wang, Q. Kang, S. Ouyang, J. Ye, *ACS Nano* **2014**, *8*, 7078 – 7087; d) W. Han, C. Zang, Z. Huang, H. Zhang, L. Ren, X. Qi, J. Zhong, *Int. J. Hydrogen Energy* **2014**, *39*, 19502 – 19512; e) Y.-J. Yuan, J.-R. Tu, Z.-J. Ye, D.-Q. Chen, B. Hu, Y.-W. Huang, T.-T. Chen, D.-P. Cao, Z.-T. Yu, Z.-G. Zou, *Appl. Catal. B* **2016**, *188*, 13 – 22.

[174] S. Cao, Y. Chen, L. Kang, Z. Lin, W.-F. Fu, *J. Mater. Chem. A* **2015**, *3*, 18711 – 18717.

[175] X.-J. Lv, W.-F. Fu, C.-Y. Hu, Y. Chen, W.-B. Zhou, *RSC Adv.* **2013**, *3*, 1753.

[176] Z. Yan, X. Yu, A. Han, P. Xu, P. Du, *J. Phys. Chem. C* **2014**, *118*, 22896 – 22903.

[177] Z. Mou, S. Yin, M. Zhu, Y. Du, X. Wang, P. Yang, J. Zheng, C. Lu, *Phys. Chem. Chem. Phys.* **2013**, *15*, 2793 – 2799.

[178] J. Hou, Z. Wang, W. Kan, S. Jiao, H. Zhu, R. V. Kumar, *J. Mater. Chem.* **2012**, *22*, 7291.

[179] J. Hou, C. Yang, H. Cheng, Z. Wang, S. Jiao, H. Zhu, *Phys. Chem. Chem. Phys.* **2013**, *15*, 15660 – 15668.

[180] B. Wang, Q. Sun, S. Liu, Y. Li, *Int. J. Hydrogen Energy* **2013**, *38*, 7232 – 7240.

[181] N. Zhang, Y. Zhang, X. Pan, M.-Q. Yang, Y.-J. Xu, *J. Phys. Chem. C* **2012**, *116*, 18023 – 18031.

[182] C. Han, Z. Chen, N. Zhang, J. C. Colmenares, Y.-J. Xu, *Adv. Funct. Mater.* **2015**, *25*, 221 – 229.

[183] J. Zhang, L. Qi, J. Ran, J. Yu, S. Z. Qiao, *Adv. Energy Mater.* **2014**, *4*, 1301925.

[184] B. Seger, I. E. Castelli, P. C. K. Vesborg, K. W. Jacobsen, O. Hansen, I. Chorkendorff, *Energy Environ. Sci.* **2014**, *7*, 2397 – 2413.

[185] a) M. G. Walter, E. L. Warren, J. R. McKone, S. W. Boettcher, Q. Mi, E. A. Santori, N. S. Lewis, *Chem. Rev.* **2010**, *110*, 6446 – 6473; b) S. Choudhary, S. Upadhyay, P. Kumar, N. Singh, V. R. Satsangi, R. Shrivastav, S. Dass, *Int. J. Hydrogen Energy* **2012**, *37*, 18713 – 18730; c) Z. Li, W. Luo, M. Zhang, J. Feng, Z. Zou, *Energy Environ. Sci.* **2013**, *6*, 347 – 370.

[186] E. S. Kim, N. Nishimura, G. Magesh, J. Y. Kim, J. W. Jang, H. Jun, J. Kubota, K. Domen, J. S. Lee, *J. Am. Chem. Soc.* **2013**, *135*, 5375 – 5383.

[187] J. Hou, C. Yang, H. Cheng, S. Jiao, O. Takeda, H. Zhu, *Energy Environ. Sci.* **2014**, *7*, 3758 – 3768.

[188] X. Chang, T. Wang, P. Zhang, J. Zhang, A. Li, J. Gong, *J. Am. Chem. Soc.* **2015**, *137*, 8356 – 8359.

[189] T. T. Guaraldo, J. F. d. Brito, D. Wood, M. V. B. Zanoni, *Electrochim. Acta* **2015**, *185*, 117 – 124.

[190] M. A. Mahadik, P. S. Shinde, M. Cho, J. S. Jang, *Appl. Catal. B* **2016**, *184*, 337 – 346.

[191] H.-i. Kim, D. Monllor-Satoca, W. Kim, W. Choi, *Energy Environ. Sci.* **2015**, *8*, 247 – 257.

[192] a) P. M. Rao, L. Cai, C. Liu, I. S. Cho, C. H. Lee, J. M. Weisse, P. Yang, X. Zheng, *Nano Lett.* **2014**, *14*, 1099 – 1105; b) J. H. Kim, G. Magesh, H. J. Kang, M. Banu, J. H. Kim, J. Lee, J. S. Lee, *Nano Energy* **2015**, *15*, 153 – 163; c) J. Su, L. Guo, N. Bao, C. A. Grimes, *Nano Lett.* **2011**, *11*, 1928 – 1933; d) A. Loiudice, J. K. Cooper, L. H. Hess, T. M. Mattox, I. D. Sharp, R. Buonsanti, *Nano Lett.* **2015**, *15*, 7347 – 7354.

[193] Y. Hou, F. Zuo, A. Dagg, P. Feng, *Angew. Chem. Int. Ed.* **2013**, *52*, 1248 – 1252; *Angew. Chem.* **2013**, *125*, 1286 – 1290.

[194] K. J. McDonald, K.-S. Choi, *Chem. Mater.* **2011**, *23*, 4863 – 4869.

[195] J. Hou, H. Cheng, O. Takeda, H. Zhu, *Energy Environ. Sci.* **2015**, *8*, 1348 – 1357.

[196] Y. Hou, F. Zuo, A. P. Dagg, J. Liu, P. Feng, *Adv. Mater.* **2014**, *26*, 5043 – 5049.

[197] M. T. Mayer, Y. Lin, G. Yuan, D. Wang, *Acc. Chem. Res.* **2013**, *46*, 1558 – 1566.

[198] L. Chen, J. Yang, S. Klaus, L. J. Lee, R. Woods-Robinson, J. Ma, Y. Lum, J. K. Cooper, F. M. Toma, L. W. Wang, I. D. Sharp, A. T. Bell, J. W. Ager, *J. Am. Chem. Soc.* **2015**, *137*, 9595 – 9603.

[199] Y. J. Hwang, A. Boukai, P. Yang, *Nano Lett.* **2009**, *9*, 410 – 415.

[200] a) M. T. Mayer, C. Du, D. Wang, *J. Am. Chem. Soc.* **2012**, *134*, 12406 – 12409; b) X. Wang, K. Q. Peng, Y. Hu, F. Q. Zhang, B. Hu, L. Li, M. Wang, X. M. Meng, S. T. Lee, *Nano Lett.* **2014**, *14*, 18 – 23.

[201] S. Fan, B. AlOtaibi, S. Y. Woo, Y. Wang, G. A. Botton, Z. Mi, *Nano Lett.* **2015**, *15*, 2721 – 2726.

[202] J. Chen, L. Zhang, Z. Lam, H. B. Tao, Z. Zeng, H. B. Yang, J. Luo, L. Ma, B. Li, J. Zheng, S. Jia, Z. Wang, Z. Zhu, B. Liu, *J. Am. Chem. Soc.* **2016**, *138*, 3183 – 189.

[203] Y. W. Chen, J. D. Prange, S. Duhnen, Y. Park, M. Gunji, C. E. Chidsey, P. C. McIntyre, *Nat. Mater.* **2011**, *10*, 539 – 544.

[204] L. Ji, M. D. McDaniel, S. Wang, A. B. Posadas, X. Li, H. Huang, J. C. Lee, A. A. Demkov, A. J. Bard, J. G. Ekerdt, E. T. Yu, *Nat. Nanotechnol.* **2015**, *10*, 84 – 90.

[205] a) S. Hu, M. R. Shaner, J. A. Beardslee, M. Lichterman, B. S. Brunschwig, N. S. Lewis, *Science* **2014**, *344*, 1005 – 1009; b) Y. Lin, C. Battaglia, M. Boccard, M. Hettick, Z. Yu, C. Ballif, J. W. Ager, A. Javey, *Nano Lett.* **2013**, *13*, 5615 – 5618.

[206] H. Jung, S. Y. Chae, C. Shin, B. K. Min, O. S. Joo, Y. J. Hwang, *ACS Appl. Mater. Interfaces* **2015**, *7*, 5788 – 5796.

[207] a) J. Bai, J. Li, Y. Liu, B. Zhou, W. Cai, *Appl. Catal. B* **2010**, *95*, 408 – 413; b) G. Ai, H. Li, S. Liu, R. Mo, J. Zhong, *Adv. Funct. Mater.* **2015**, *25*, 5706 – 5713.

[208] a) J. Hensel, G. Wang, Y. Li, J. Z. Zhang, *Nano Lett.* **2010**, *10*, 478 – 483; b) J. Luo, L. Ma, T. He, C. F. Ng, S. Wang, H. Sun, H. J. Fan, *J. Phys. Chem. C* **2012**, *116*, 11956 – 11963.

[209] Y.-L. Lee, C.-F. Chi, S.-Y. Liau, *Chem. Mater.* **2010**, *22*, 922 – 927.
[210] N. Srinivasan, Y. Shiga, D. Atarashi, E. Sakai, M. Miyauchi, *Appl. Catal. B* **2015**, *179*, 113 – 121.
[211] S. Cheng, W. Fu, H. Yang, L. Zhang, J. Ma, H. Zhao, M. Sun, L. Yang, *J. Phys. Chem. C* **2012**, *116*, 2615 – 2621.
[212] a) X. Li, Z. Zhang, L. Chen, Z. Liu, J. Cheng, W. Ni, E. Xie, B. Wang, *J. Power Sources* **2014**, *269*, 866 – 872; b) C. Gao, Z. Zhang, X. Li, L. Chen, Y. Wang, Y. He, F. Teng, J. Zhou, W. Han, E. Xie, *Sol. Energy Mater. Sol. Cells* **2015**, *141*, 101 – 107.
[213] M. Seol, J.-W. Jang, S. Cho, J. S. Lee, K. Yong, *Chem. Mater.* **2013**, *25*, 184 – 189.
[214] C.-J. Lin, L.-C. Kao, Y. Huang, M. A. Bañares, S. Y.-H. Liou, *Int. J. Hydrogen Energy* **2015**, *40*, 1388 – 1393.
[215] J. Han, Z. Liu, K. Guo, B. Wang, X. Zhang, T. Hong, *Appl. Catal. B* **2015**, *163*, 179 – 188.
[216] Y. Li, X. Zhang, S. Jiang, H. Dai, X. Sun, Y. Li, *Sol. Energy Mater. Sol. Cells* **2015**, *132*, 40 – 46.
[217] H. Xu, R. Mo, C. Cheng, G. Ai, Q. Chen, S. Yang, H. Li, J. Zhong, *RSC Adv.* **2014**, *4*, 47429 – 47435.
[218] H. Kim, M. Seol, J. Lee, K. Yong, *J. Phys. Chem. C* **2011**, *115*, 25429 – 25436.
[219] G. Wang, X. Yang, F. Qian, J. Z. Zhang, Y. Li, *Nano Lett.* **2010**, *10*, 1088 – 1092.
[220] a) W. Hou, S. B. Cronin, *Adv. Funct. Mater.* **2013**, *23*, 1612 – 1619; b) Y. C. Pu, G. Wang, K. D. Chang, Y. Ling, Y. K. Lin, B. C. Fitzmorris, C. M. Liu, X. Lu, Y. Tong, J. Z. Zhang, Y. J. Hsu, Y. Li, *Nano Lett.* **2013**, *13*, 3817 – 3823; c) X. Wang, C. Liow, A. Bisht, X. Liu, T. C. Sum, X. Chen, S. Li, *Adv. Mater.* **2015**, *27*, 2207 – 2214; d) I. Thomann, B. A. Pinaud, Z. Chen, B. M. Clemens, T. F. Jaramillo, M. L. Brongersma, *Nano Lett.* **2011**, *11*, 3440 – 3446; e) Z. Zhang, L. Zhang, M. N. Hedhili, H. Zhang, P. Wang, *Nano Lett.* **2013**, *13*, 14 – 20; f) S. C. Warren, E. Thimsen, *Energy Environ. Sci.* **2012**, *5*, 5133 – 5146; g) J. Li, S. K. Cushing, P. Zheng, T. Senty, F. Meng, A. D. Bristow, A. Manivannan, N. Wu, *J. Am. Chem. Soc.* **2014**, *136*, 8438 – 8449.
[221] Z. Liu, W. Hou, P. Pavaskar, M. Aykol, S. B. Cronin, *Nano Lett.* **2011**, *11*, 1111 – 1116.
[222] X. Zhang, Y. Liu, S.-T. Lee, S. Yang, Z. Kang, *Energy Environ. Sci.* **2014**, *7*, 1409.
[223] a) X. Zhang, Y. Li, J. Zhao, S. Wang, Y. Li, H. Dai, X. Sun, *J. Power Sources* **2014**, *269*, 466 – 472; b) Y.-G. Lin, Y.-K. Hsu, Y.-C. Chen, S.-B. Wang, J. T. Miller, L.-C. Chen, K.-H. Chen, *Energy Environ. Sci.* **2012**, *5*, 8917.
[224] C. Li, X. T. Zhu, H. F. Zhang, Z. C. Zhu, B. Liu, C. W. Cheng, *Adv. Mater. Interfaces* **2015**, *2*, 1500428.
[225] a) S. A. Mann, E. C. Garnett, *Nano Lett.* **2013**, *13*, 3173 – 3178; b) L. Zhou, X. Yu, J. Zhu, *Nano Lett.* **2014**, *14*, 1093 – 1098.
[226] S. Ramadurgam, T. G. Lin, C. Yang, *Nano Lett.* **2014**, *14*, 4517 – 4522.
[227] a) S. Mubeen, J. Lee, N. Singh, S. Kramer, G. D. Stucky, M. Moskovits, *Nat. Nanotechnol.* **2013**, *8*, 247 – 251; b) J. Lee, S. Mubeen, X. Ji, G. D. Stucky, M. Moskovits, *Nano Lett.* **2012**, *12*, 5014 – 5019; c) H. J. Kim, S. H. Lee, A. A. Upadhye, I. Ro, M. I. Tejedor-Tejedor, M. A. Anderson, W. B. Kim, G. W. Huber, *ACS Nano* **2014**, *8*, 10756 – 10765.
[228] L. J. Minggu, W. R. Wan Daud, M. B. Kassim, *Int. J. Hydrogen Energy* **2010**, *35*, 5233 – 5244.
[229] A. C. Nielander, M. R. Shaner, K. M. Papadantonakis, S. A. Francis, N. S. Lewis, *Energy Environ. Sci.* **2015**, *8*, 16 – 25.
[230] a) M. S. Prévot, K. Sivula, *J. Phys. Chem. C* **2013**, *117*, 17879 – 17893; b) T. J. Jacobsson, V. Fjallstrom, M. Edoff, T. Edvinsson, *Energy Environ. Sci.* **2014**, *7*, 2056 – 2070; c) X. Peng, C. He, X. Fan, Q. Liu, J. Zhang, H. Wang, *Int. J. Hydrogen Energy* **2014**, *39*, 14166 – 14171.
[231] a) M. M. May, H. J. Lewerenz, D. Lackner, F. Dimroth, T. Hannappel, *Nat. Commun.* **2015**, *6*, 8286; b) S. Hu, N. S. Lewis, J. W. Ager, J. Yang, J. R. McKone, N. C. Strandwitz, *J. Phys. Chem. C* **2015**, *119*, 24201 – 24228; c) E. Verlage, S. Hu, R. Liu, R. J. R. Jones, K. Sun, C. Xiang, N. S. Lewis, H. A. Atwater, *Energy Environ. Sci.* **2015**, *8*, 3166 – 3172.
[232] O. Khaselev, *Science* **1998**, *280*, 425 – 427.
[233] a) W. Calvet, E. Murugasen, J. Klett, B. Kaiser, W. Jaegermann, F. Finger, S. Hoch, M. Blug, J. Busse, *Phys. Chem. Chem. Phys.* **2014**, *16*, 12043 – 12050; b) F. Urbain, V. Smirnov, J.-P. Becker, A. Lambertz, F. Yang, J. Ziegler, B. Kaiser, W. Jaegermann, U. Rau, F. Finger, *Energy Environ. Sci.* **2016**, *9*, 145 – 154; c) L. Han, I. A. Digdaya, T. W. F. Buijs, F. F. Abdi, Z. Huang, R. Liu, B. Dam, M. Zeman, W. A. Smith, A. H. M. Smets, *J. Mater. Chem. A* **2015**, *3*, 4155 – 4162; d) L. Han, F. F. Abdi, P. Perez Rodriguez, B. Dam, R. van de Krol, M. Zeman, A. H. Smets, *Phys. Chem. Chem. Phys.* **2014**, *16*, 4220 – 4229; e) L. Han, F. F. Abdi, R. van de Krol, R. Liu, Z. Huang, H. J. Lewerenz, B. Dam, M. Zeman, A. H. Smets, *ChemSusChem* **2014**, *7*, 2832 – 2838; f) H. P. Wang, K. Sun, S. Y. Noh, A. Kargar, M. L. Tsai, M. Y. Huang, D. Wang, J. H. He, *Nano Lett.* **2015**, *15*, 2817 – 2824.
[234] a) C. R. Cox, J. Z. Lee, D. G. Nocera, T. Buonassisi, *Proc. Natl. Acad. Sci. USA* **2014**, *111*, 14057 – 14061; b) M. T. Winkler, C. R. Cox, D. G. Nocera, T. Buonassisi, *Proc. Natl. Acad. Sci. USA* **2013**, *110*, E1076 – E1082; c) T. J. Jacobsson, V. Fjällström, M. Edoff, T. Edvinsson, *Sol. Energy Mater. Sol. Cells* **2015**, *134*, 185 – 193.
[235] a) J. Brillet, M. Cornuz, F. L. Formal, J.-H. Yum, M. Grätzel, K. Sivula, *J. Mater. Res.* **2010**, *25*, 17 – 24; b) J. Brillet, J.-H. Yum, M. Cornuz, T. Hisatomi, R. Solarska, J. Augustynski, M. Graetzel, K. Sivula, *Nat. Photonics* **2012**, *6*, 824 – 828.
[236] V. González-Pedro, I. Zarazua, E. M. Barea, F. Fabregat-Santiago, E. de La Rosa, I. Mora-Seró, S. Giménez, *J. Phys. Chem. C* **2014**, *118*, 891 – 895.
[237] a) K. Shin, J.-B. Yoo, J. H. Park, *J. Power Sources* **2013**, *225*, 263 – 268; b) J. K. Kim, K. Shin, S. M. Cho, T.-W. Lee, J. H. Park, *Energy Environ. Sci.* **2011**, *4*, 1465.
[238] a) Y. S. Chen, J. S. Manser, P. V. Kamat, *J. Am. Chem. Soc.* **2015**, *137*, 974 – 981; b) C. G. Morales-Guio, M. T. Mayer, A. Yella, S. D. Tilley, M. Grätzel, X. Hu, *J. Am. Chem. Soc.* **2015**, *137*, 9927 – 9936; c) X. Zhang, B. Zhang, K. Cao, J. Brillet, J. Chen, M. Wang, Y. Shen, *J. Mater. Chem. A* **2015**, *3*, 21630 – 21636; d) Gurudayal, D. Sabba, M. H. Kumar, L. H. Wong, J. Barber, M. Grätzel, N. Mathews, *Nano Lett.* **2015**, *15*, 3833 – 3839; e) P. Dias, M. Schreier, S. D. Tilley, J. S. Luo, J. Azevedo, L. Andrade, D. Q. Bi, A. Hagfeldt, A. Mendes, M. Grätzel, M. T. Mayer, *Adv. Energy Mater.* **2015**, *5*, 1501537.
[239] J. Luo, J. H. Im, M. T. Mayer, M. Schreier, M. K. Nazeeruddin, N. G. Park, S. D. Tilley, H. J. Fan, M. Grätzel, *Science* **2014**, *345*, 1593 – 1596.
[240] P. Da, M. Cha, L. Sun, Y. Wu, Z. S. Wang, G. Zheng, *Nano Lett.* **2015**, *15*, 3452 – 3457.
[241] a) B. AlOtaibi, S. Fan, S. Vanka, M. G. Kibria, Z. Mi, *Nano Lett.* **2015**, *15*, 6821 – 6828; b) H. B. Yang, J. Miao, S. F. Hung, F. Huo, H. M. Chen, B. Liu, *ACS Nano* **2014**, *8*, 10403 – 10413.
[242] S. K. Mohapatra, M. Misra, V. K. Mahajan, K. S. Raja, *J. Phys. Chem. C* **2007**, *111*, 8677 – 8685.
[243] Z. Wu, G. Zhao, Y. Zhang, J. Liu, Y. N. Zhang, H. Shi, *J. Mater. Chem. A* **2015**, *3*, 3416 – 3424.
[244] H. Wang, J. A. Turner, *J. Electrochem. Soc.* **2010**, *157*, F173.
[245] Y. Wang, J. Tang, Z. Peng, Y. Wang, D. Jia, B. Kong, A. A. Elzatahry, D. Zhao, G. Zheng, *Nano Lett.* **2014**, *14*, 3668 – 3673.
[246] Y. Fujishima, S. Okamoto, M. Yoshiba, T. Itoi, S. Kawamura, Y. Yoshida, Y. Ogura, Y. Izumi, *J. Mater. Chem. A* **2015**, *3*, 8389 – 8404.
[247] R. Raja, P. Sudhagar, A. Devadoss, C. Terashima, L. K. Shrestha, K. Nakata, R. Jayavel, K. Ariga, A. Fujishima, *Chem. Commun.* **2015**, *51*, 522 – 525.
[248] P. Bornoz, F. F. Abdi, S. D. Tilley, B. Dam, R. van de Krol, M. Grätzel, K. Sivula, *J. Phys. Chem. C* **2014**, *118*, 16959 – 16966.
[249] J.-W. Jang, C. Du, Y. Ye, Y. Lin, X. Yao, J. Thorne, E. Liu, G. McMahon, J. Zhu, A. Javey, J. Guo, D. Wang, *Nat. Commun.* **2015**, *6*, 7447.
[250] C. Ding, W. Qin, N. Wang, G. Liu, Z. Wang, P. Yan, J. Shi, C. Li, *Phys. Chem. Chem. Phys.* **2014**, *16*, 15608 – 15614.
[251] S. Sato, T. Arai, T. Morikawa, K. Uemura, T. M. Suzuki, H. Tanaka, T. Kajino, *J. Am. Chem. Soc.* **2011**, *133*, 15240 – 15243.
[252] G. Magesh, E. S. Kim, H. J. Kang, M. Banu, J. Y. Kim, J. H. Kim, J. S. Lee, *J. Mater. Chem. A* **2014**, *2*, 2044.
[253] a) S. Hu, C. Xiang, S. Haussener, A. D. Berger, N. S. Lewis, *Energy Environ. Sci.* **2013**, *6*, 2984; b) J. Zhao, X. Wang, Z. Xu, J. S. C. Loo, *J. Mater. Chem. A* **2014**, *2*, 15228; c) J. Cheng, M. Zhang, G. Wu, X. Wang, J. Zhou, K. Cen, *Sol. Energy Mater. Sol. Cells* **2015**, *132*, 606 – 614; d) A. J. Nozik, *Appl. Phys. Lett.* **1977**, *30*, 567; e) J. Cheng, M. Zhang, G. Wu, X. Wang, J. Zhou, K. Cen, *Environ. Sci. Technol.* **2014**, *48*, 7076 – 7084; f) G. K. Mor, O. K. Varghese, R. H. T. Wilke, S. Sharma, K. Shankar, T. J. Latempa, K.-S. Choi, C. A. Grimes, *Nano Lett.* **2008**, *8*, 1906 – 1911; g) K. Shankar, J. I. Basham, N. K. Allam, O. K. Varghese, G. K. Mor, X. J. Feng, M. Paulose, J. A. Seabold, K. S. Choi, C. A. Grimes, *J. Phys. Chem. C* **2009**, *113*, 6327 – 6359; h) T. Arai, S. Sato, T. Kajino, T. Morikawa, *Energy Environ. Sci.* **2013**, *6*, 1274; i) C. Ampelli, G. Centi, R. Passalacqua, S. Perathoner, *Energy Environ. Sci.* **2010**, *3*, 292; j) S. Y. Reece, J. A. Hamel,

K. Sung, T. D. Jarvi, A. J. Esswein, J. J. Pijpers, D. G. Nocera, *Science* **2011**, *334*, 645 – 648; k) Y. Zhong, K. Ueno, Y. Mori, X. Shi, T. Oshikiri, K. Murakoshi, H. Inoue, H. Misawa, *Angew. Chem. Int. Ed.* **2014**, *53*, 10350 – 10354; *Angew. Chem.* **2014**, *126*, 10518 – 10522.

[254] S. Mubeen, J. Lee, N. Singh, M. Moskovits, E. W. McFarland, *Energy Environ. Sci.* **2013**, *6*, 1633.

[255] S. Haussener, C. Xiang, J. M. Spurgeon, S. Ardo, N. S. Lewis, A. Z. Weber, *Energy Environ. Sci.* **2012**, *5*, 9922.

[256] R. E. Rocheleau, E. L. Miller, A. Misra, *Energy Fuels* **1998**, *12*, 3 – 10.

[257] Y. Qu, L. Liao, R. Cheng, Y. Wang, Y. C. Lin, Y. Huang, X. Duan, *Nano Lett.* **2010**, *10*, 1941 – 1949.

[258] a) H. S. Jeon, J. H. Koh, S. J. Park, M. S. Jee, D.-H. Ko, Y. J. Hwang, B. K. Min, *J. Mater. Chem. A* **2015**, *3*, 5835 – 5842; b) T. Arai, S. Sato, T. Morikawa, *Energy Environ. Sci.* **2015**, *8*, 1998 – 2002.

[259] S. Sato, T. Arai, T. Morikawa, *Inorg. Chem.* **2015**, *54*, 5105 – 5113.

[260] a) M. B. McDonald, S. Ardo, N. S. Lewis, M. S. Freund, *ChemSusChem* **2014**, *7*, 3021 – 3027; b) M. B. McDonald, J. P. Bruce, K. McEleney, M. S. Freund, *ChemSusChem* **2015**, *8*, 2645 – 2654.

[261] a) S. Mubeen, N. Singh, J. Lee, G. D. Stucky, M. Moskovits, E. W. McFarland, *Nano Lett.* **2013**, *13*, 2110 – 2115; b) N. M. Vargas-Barbosa, G. M. Geise, M. A. Hickner, T. E. Mallouk, *ChemSusChem* **2014**, *7*, 3017 – 3020; c) J. M. Spurgeon, M. G. Walter, J. Zhou, P. A. Kohl, N. S. Lewis, *Energy Environ. Sci.* **2011**, *4*, 1772; d) J. Rongé, D. Nijs, S. Kerkhofs, K. Maschaele, J. A. Martens, *Phys. Chem. Chem. Phys.* **2013**, *15*, 9315 – 9325; e) S. Ichikawa, R. Doi, *Catal. Today* **1996**, *27*, 271 – 277.

[262] H. B. Gray, *Nat. Chem.* **2009**, *1*, 7.

[263] a) S. L. McFarlane, B. A. Day, K. McEleney, M. S. Freund, N. S. Lewis, *Energy Environ. Sci.* **2011**, *4*, 1700; b) J. M. Spurgeon, S. W. Boettcher, M. D. Kelzenberg, B. S. Brunschwig, H. A. Atwater, N. S. Lewis, *Adv. Mater.* **2010**, *22*, 3277 – 3281.

[264] D. Kang, T. W. Kim, S. R. Kubota, A. C. Cardiel, H. G. Cha, K. S. Choi, *Chem. Rev.* **2015**, *115*, 12839 – 12887.

Received: June 10, 2016
Published online on ■■ ▮▮, 0000

*G. Liu, K. Du, S. Haussener, K. Wang**

■■ – ■■

Charge Transport in Two-Photon Semiconducting Structures for Solar Fuels

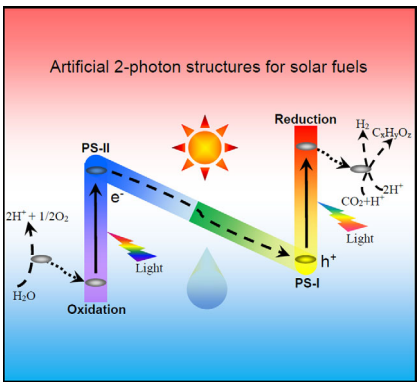

Burning bright: Progress on two-photon semiconducting structures is presented with focus on understanding of interfacial carrier dynamics. Strategies from solution-particle photocatalytic systems to nanostructured photoelectrode and photoelectrochemical devices are discussed to elucidate the mechanism of charge transport and to rationalize experimental observations. The studies compile valuable knowledge to build efficient solar-driven systems for clean energy.